ABSTRACT

HYKES, JOSHUA M. Verification and Validation of Radiation Transport Numerical Methods, Codes, and Nuclear Data for Estimating Radiation Dose to Patients. (Under the direction of Dr. Yousry Azmy).

Computed tomography (CT) is an invaluable diagnostic tool in current medical practice. Unfortunately, the radiation dose imparted during a CT scan can be significant. This thesis seeks to develop, verify, and validate appropriate computational methods for computing this dose accurately and efficiently. The components of the model are the nuclear data, transport methods, and computer codes. Monte Carlo transport methods are employed primarily for their ability to accurately capture most of the relevant physical phenomena. Deterministic transport methods are subsequently verified and validated. The work is divided into three stages: experimental, verification, and validation. The experimental stage involves gathering high-fidelity data to aid in the validation procedures. Multiple radiation detection devices are employed to give greater certainty to the results. In addition, an important task is gathering data using a geometrically simplified phantom which is easier to model than the detailed Rando phantom. Towards this end, a CTDI FDA phantom is imaged. Exposure and dose measurements were taken in air and in the phantom center and periphery. The second stage, verification, involves the testing of the deterministic model for correctness of the methodology and the physics data, i.e. cross section library. Primarily, there are a few key assumptions which must be tested. The first is the importance of the secondary electron transport. Using Monte Carlo methods, it is found that the transport is unimportant for the accurate computation of the dose deposition distribution given the relatively low energy photons produced by x-rays tubes employed in CT scan machines. This makes the deterministic transport calculations much simpler. Next, the discretization of space, energy, and angle in the deterministic model is examined to ensure sufficient refinement capable of delivering accurate results. The Monte Carlo method is an excellent complement to deterministic methods, serving as reference as though it were an actual experiment, thus allowing the testing of these issues in a straightforward and highly controlled manner. In each discretization, the deterministic model proved capable, although some flux spectrum results differed by fifteen percent or more, mostly a result of the multigroup cross section set. Finally, after ensuring that the deterministic model was

functioning as expected, a comparison was made of the simulations to the experimentally measured data. This was the most difficult of the tasks, in great part because of the lack of precise knowledge of detailed information concerning some of the parameters comprising the experimental setup. However, much effort was placed into conforming the simulations to the experiment as closely as possible. The ratio of exposures in the CTDI FDA phantom periphery-to-center is computed to within experimental uncertainty of about ten percent, while the absolute computed exposures have greater errors. The absolute exposures differed from the measured values by less than 35 percent.

Verification and Validation of Radiation Transport Numerical Methods, Codes, and Nuclear Data for Estimating Radiation Dose to Patients

by
Joshua Michael Hykes

A thesis submitted to the Graduate Faculty of
North Carolina State University
in partial fullfillment of the
requirements for the Degree of
Master of Science

Nuclear Engineering

Raleigh, North Carolina

2009

APPROVED BY:

Dr. Z. Li	Dr. D. Y. Anistratov

Dr. Y. Y. Azmy
Chair of Advisory Committee

DEDICATION

Soli Deo gloria. To God alone be the glory.

BIOGRAPHY

Joshua Hykes was born in Lancaster, Pennsylvania to Michael and BJ Hykes. He attended Kraybill Mennonite School through eighth grade and then went to Lancaster Mennonite High School. After high school, he attended Penn State University where he obtained a BS in nuclear engineering. He then moved to Raleigh to attend graduate school at NC State. During the summers, he had the opportunities to work at Exelon Nuclear, Idaho National Lab, and Los Alamos National Lab.

ACKNOWLEDGMENTS

First and foremost, thanks goes to my advisor, Dr. Azmy. He graciously guided me through the entire thesis process. In addition, I appreciate the willingness of Drs. Anistratov and Li to serve on my committee. The radiology staff at Hershey Medical Center provided much assistance in the practical aspects of the project. Particularly, Ken Miller, Steve King, and Mike Erdman were instrumental in coordinating the experiments. Jesse Klingensmith began this project and provided NJOY expertise.

Finally, I appreciate the support of my parents and the care of my wife Beth. This thesis might have proved impossible without the rejuvinating power of her brownies.

TABLE OF CONTENTS

LIST OF TABLES

LIST OF FIGURES

Chapter 1

Review of Related Work

The radiation dose from CT scans is an important safety concern, prompting much research into both experimental and computational means to estimate the dose to patients. When one further considers similar work for other radiographic medical procedures, a large body of research exists on radiation dose from medical x-rays. Much practical guidance is available in the literature, as well as in more abstract subjects such as computational radiation transport. Within computational transport methods, great effort has been devoted to applying Monte Carlo methods to successfully predict radiation dose to patients. Less research has been dedicated to the application of deterministic methods to medical diagnostic imaging, although recent work has made progress in this area.

This chapter is devoted to understanding the broader framework in which the current work resides. The chapter begins with some historical notes on CT scans and their use by the medical community. Next, common physical concepts and definitions are presented which are necessary when considering the practices and risks associated with CT scans. Typical radiation doses for a variety of medical and non-medical events are given. The risks of CT scan radiation dose are discussed. This is followed by a description of what factors influence absorbed dose, and what can be done to minimize it. The earlier experiment performed at the Hershey Medical Center is reviewed. Finally, details are given about previous work related to modeling medical radiation doses computationally.

1.1 Computed Tomography

1.1.1 CT Scan History

When Wilhelm Röntgen, a German physics professor, discovered x-rays in 1895, the potential to peer into the human body was immediately obvious [2]. Röntgen's publication "On a new kind of rays" included a number of pictures exposed with these rays. One of the pictures showed the bones of his wife's hand, along with a ring she was wearing (see Figure 1.1). *Projection radiography*, the capture of a two-dimensional projected view of the body's internals, is still the most commonly used tool for medical diagnosis [3]. In addition to projection radiography, numerous other technologies using x-rays have been developed to gain a more detailed description of the patient's anatomy. Computed tomography is one of the powerful imaging modalities developed which leverages the discovery made by Röntgen.

Figure 1.1: A famous radiographic image taken by Wilhem Röntgen of his wife Anna Bertha's hand in 1895.

Godrey N. Hounsfield introduced the first computed tomographic system for clinical use in 1972 at the Atkinson Morley Hospital in London [4]. Working as an engineer in Britain, he independently developed the necessary theory and technology. However, two previous individuals had laid the essential theoretical framework by the time Hounsfield had begun his work. The mathematician J. H. Radon made the most fundamental contribution

for the reconstruction of the image [5], proving that the distribution of a property in an object can be determined with an infinite number of integral measurements through that object. Although Radon's work says little about current algorithms for image reconstruction, the theory he developed provided the groundwork for future implementations.

In contrast to the infinite number of projections assumed by Radon, only a discrete, finite set of projections is available in CT. In the southern hemisphere, working on what he later described as a hobby, A. M. Cormack developed a method to perform the reconstruction for a discrete set of points (x_i, y_j) with a finite set of projections [4]. He had become interested in the idea at Groote Schur Hospital while attending the University of Cape Town in South Africa. After developing the theory from 1957 to 1963, he never pursued the construction of such a machine. In recognition of the efforts of Cormack and Hounsfield in developing computed tomography, the pair received the Nobel Prize for Medicine in 1979.

Computed tomography has benefited immensely from the growth of inexpensive digital computing power. The first machine made by Hounsfield, called the EMI Mark 1, required 4.5 minutes for the imaging of each slice, and another 1.5 minutes for the image reconstruction of that slice. The machine produced an image with 80-by-80 pixels [3]. Modern CT scanners operate in fractions of a second, producing images with 1024-by-1024 pixels.

Given the rapid technological improvements and the clear diagnostic benefits, CT scans have enjoyed widespread adoption since their introduction in 1972 [6]. The growth in the technology's use is evident, going from 3.6 million scans in 1980 to 62 million in the year 2006 in the United States, as seen in Figure 1.2.

1.1.2 Image Generation

Constructing a two-dimensional image from a series of one-dimensional line measurements is the distinctive feature of CT as compared to traditional projection radiography. The line measurements are made using x-rays, where the linear attenuation coefficient is the property being measured. As stated previously, the Austrian mathematician Radon proved that this was theoretically possible. His 1917 paper "On the determination of functions from their integrals along certain manifolds" is regarded as the seminal work in the field [5]. Radon proved that the distribution of properties in an object can be determined given

Year	Millions of CT Scans
1980	3.6
1990	13.3
1997	27
1998	33
2000	46
2006	62

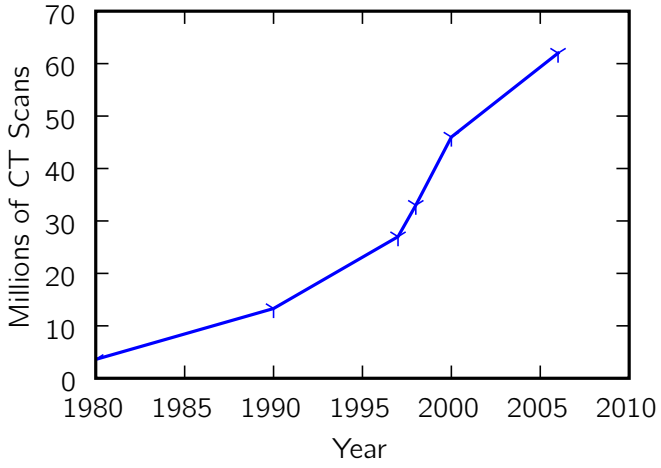

Figure 1.2: CT scan procedures have become much more frequent since their introduction in 1972 [6, 7, 8].

an infinite number of integral measurements through that object. Formally, the material property unknown is a function $f(x, y)$, where two spatial dimensions are considered. The two-dimensional Radon transform of f is [9]

$$g(l, \theta) = \int_{-\infty}^{\infty} f(x(s), y(s))\, ds, \tag{1.1}$$

where

$$x(s) = l\cos\theta - s\sin\theta,$$
$$y(s) = l\sin\theta + s\cos\theta.$$

Equation (1.1) is a projection on the line with angle θ from the y-axis and distance l from the origin. In the case of CT, the distributed 2-D function is the linear attenuation coefficient $\mu(x, y)$. The *projection-slice theorem* states that the 1-D Fourier transform with respect to l of the projection $g(l, \theta)$ is equal to a line at the same angle θ through the 2-D Fourier transform of the distribution. Thus, taking the 2-D inverse Fourier transform of the 1-D Fourier transform of the projection yields the desired distribution function:

$$f(x, y) = \mathcal{F}_{2D}^{-1}\{G(\rho, \theta)\}, \tag{1.2}$$

where $G(\rho, \theta)$ is the 1-D Fourier transform of $g(l, \theta)$ [9]. While theoretically possible, this is not a practical means to perform the inversion in CT machines.

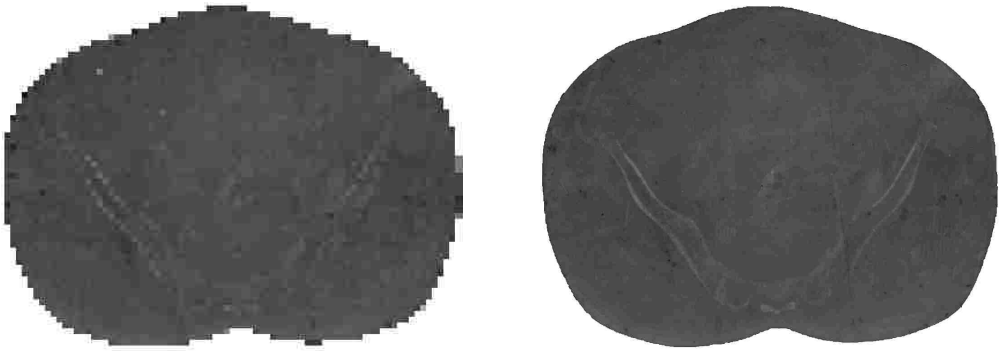

(a) 80x80 pixels. (b) 1024x1024 pixels.

Figure 1.3: The effect of pixel count on image quality.

There are many different reconstruction techniques available. An early algorithm was the *algebraic reconstruction technique*, which builds a system of N equations for N pixel unknowns. This system is solved iteratively. However, the solution has a high computational cost. This prompted researchers to pursue other algorithms, such as backprojection and Fourier methods [4]. Fourier methods are extensions of Equation (1.2), where some algebraic manipulation and intermediate filters improve upon a pure Fourier inversion. Backprojection methods are also common. The premise of such algorithms is that the projected measurement for each line can be smeared back along that line. The smeared data is then summed over all the projections. Unfortunately, a simple backprojection introduces unnatural artifacts. To eliminate these errors, a filtering or convolution step is also included. At present, filtered-backprojection is the most commonly employed reconstruction algorithm in clinical use [3].

Regardless of the algorithm chosen, the final image of the slice is a matrix of values for the linear attenuation coefficient. The image is reconstructed as a matrix of pixels, or picture elements. In 1974, brain CT scans had 80-by-80 pixel images [4]. This pixelated image was a rather fuzzy representation of the analog picture. However, with a greater number of pixels produced today, usually 1024-by-1024, the pixels become indistinguishable to the human eye. Figure 1.3 shows one such example of this phenomenon.

1.1.3 Mechanics of CT

Modern CT machines are complex and proprietary. For the purposes of the initial validation contained in this thesis, only a few of the essential details are discussed here. The main concern is how individual slices are imaged. A secondary question is how the machine acquires multiple slices.

To scan a single slice, the CT machine takes a collection of projection measurements with a rotating x-ray beam to obtain the perspectives needed to construct the two-dimensional image. An array of detectors is positioned on the opposing side of the patient from the x-ray source to measure the radiation intensity exiting the patient. Nearly all current designs have the detectors rotate in concert with the x-ray tube. Early machines used parallel x-ray beams by translating the x-ray tube in addition to rotating it. However, modern designs call for only rotation with a fan-shaped beam [4]. Figure 1.4*a* shows the fan beam in a cross section view of the machine. Since the beam spreads, it intersects with the entire body, giving more projection data in the same amount of time. Collimators shape the beam to the desired geometry, and filters selectively reduce the beam intensity. Since the cross sections for the absorption of photons drastically increases at low energies, the low-energy photons are preferentially absorbed by the filters. Since these photons have a high probability of absorption in the patient, they make a significant contribution to the dose without adding to the image quality. Thus, reducing them in a filter is a common practice. This reduction in low-energy photons is discussed in Section 1.2.1.

One other important detail in CT filters is the *bow tie* filter. The purpose of this filter is to reduce the intensity of the x-rays on the edges of the fan beam. Since the edge of the beam travels through shorter trajectories within the patient, a lower intensity can still produce the same detector response as compared to the center. This technique significantly reduces skin dose. Also, the bow tie filter is an important part of an accurate computer simulation, as will be established later.

Although the methods for obtaining multiple slices is not as central to this work, a few details are helpful. First, the slice width is determined by the collimation of the x-ray beam. The pitch determines how these slices fit together. The *pitch* is the distance of travel along the axis of rotation (of the x-ray tube) per one rotation of the x-ray tube divided by the nominal scan width [10]. If the pitch is less than 1.0, the slices are overlapping. If

it is greater than 1.0, gaps exist between the slices. For the pitch equal to 1.0, slices are adjacent and non-overlapping.

Second, the manner in which the acquisition of many slices is achieved has been the subject of innovation. Two common designs are the *axial* and *helical*, also referred to as *spiral*, scans. In the axial CT scan, the earlier of the two techniques, a full rotation of the x-ray beam is performed on one distinct slice of the subject. Then the patient is moved a short distance along the axis of rotation, the patient is brought to rest, and the next slice is acquired. In the more innovative and complex approach of helical scanning, the patient moves continuously through the x-ray beam as the x-ray tube rotates. The computer software algorithms do the work of uncurling the data into the same three-dimensional image. Spiral CT has renewed interest in computed tomography. It is useful for angiography and multiphase imaging of the liver [11]. One of the benefits of spiral CT is the increased speed, since frequent stopping and starting is unnecessary. A more recent development is the increased deployment of multi-slice scanners. Instead of having one row of detectors, these machines stack multiple rows together. The number of rows of detectors, and thus slices that can be imaged simultaneously, has increased rapidly. The motivation for this emphasis is greater axial resolution and larger scan volumes in a shorter time. This has even allowed the imaging of the beating heart with little motion artifacts in the image [4].

1.2 Photon Physics

X-rays, high energy photons compared to visible light, i.e. tens of keV, are the key ingredient in a CT scanner. They allow the radiologist to peer through flesh and bone. They also can inflict damage to tissue. This section discusses some of the important characteristics of x-rays—mainly their generation and their subsequent interactions with matter.

1.2.1 X-ray Production

The CT machine needs a reliable, strong beam of x-rays. Many different atomic-scale reactions and interactions produce x-rays, including radioisotope sources, nuclear reactors, and particle accelerators. Accelerating electrons happens to be the best method for medical x-rays. The electrons are accelerated in an evacuated tube from the negatively-

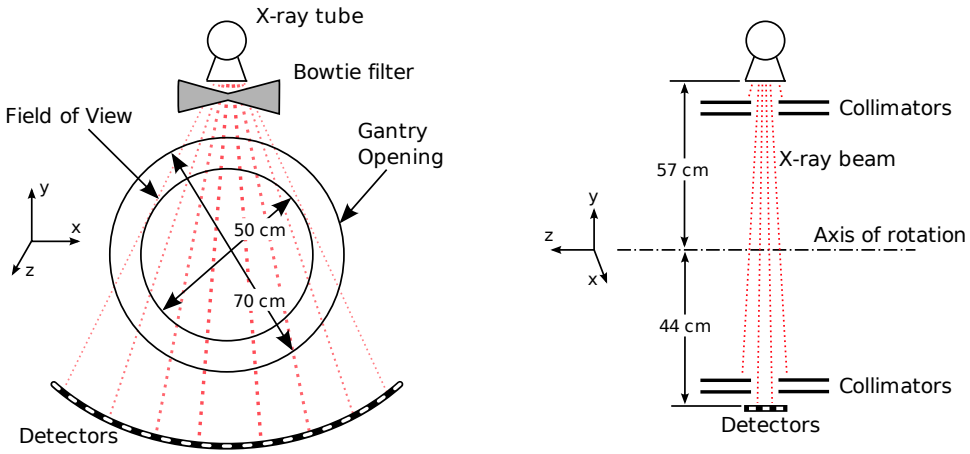

(a) CT cross section.

(b) CT axial view.

Figure 1.4: The essential structure of the CT machine. The dimensions are typical of most CT machines [4].

charged cathode to the positively-charged anode, where they collide and produce x-rays. X-ray tubes have a number of advantages. First, they can be turned on at will, and the energy of the x-rays can be adjusted by adjusting the input voltage drop between the cathode and anode. In addition, the x-rays are emitted with a directional bias. This reduces the collimation and shielding, as well as improving efficiency.

However, there are a number of problems with x-ray tubes. The first is the poor efficiency of generating x-rays using accelerated electrons. Only about 0.5% of the electrical power input to the tube goes toward the creation of x-rays [3]. The remainder is wasted as heat. Removing the heat from the tube is one of the main design concerns for x-ray tubes. This is one reason why the anode is typically made of tungsten, since it has a high melting point. The heat load and electron bombardment takes a heavy toll on the anode. Thus, x-ray tubes in a CT scanner often require replacement in less than a year [9]. Given the considerable cost of a single x-ray tube, the continued maintenance of a CT scanner is not cheap.

Figure 1.5 shows the main components of an x-ray tube. Surface electrons are released from the heated cathode filament in *thermionic emission*. These electrons are then accelerated through the potential difference. They strike the anode, mostly producing heat.

However, when the electron stops quickly, a photon is emitted. This is braking radiation or *bremsstrahlung*, in which the deceleration of the charged particle emits photons [1]. As Figure 1.6 illustrates, the bremsstrahlung radiation has its highest intensity at low energies, and monotonically decreases to the highest energy x-rays, which have energy equal to the applied tube potential. In addition to the bremsstrahlung radiation, characteristic x-rays are also possible, depending on the tube potential and the target material. In the production of characteristic x-rays, the accelerated electron displaces an inner K shell atomic electron. When other electrons transition from outer shells, a characteristic photon is emitted. For tungsten, 59.3 keV x-rays are produced in the K to L shell transition [3]. The electrical current pushed through the tube determines the number of x-rays produced per unit time. Thus, the time that the tube operates multiplied by the current gives an indication of the total number of x-ray photons produced within the x-ray tube.

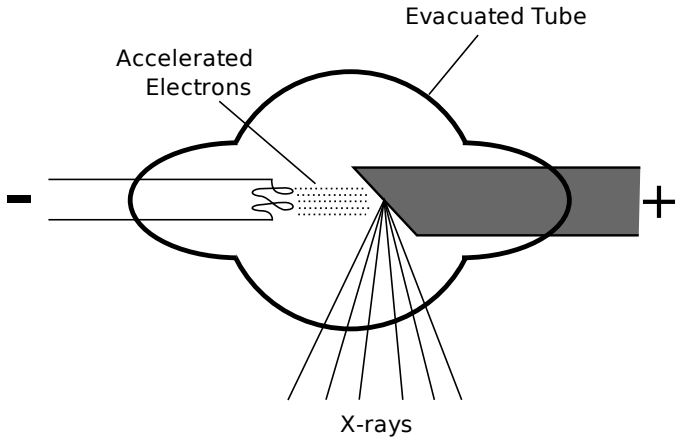

Figure 1.5: A diagram of an x-ray tube.

1.2.2 Photon Interactions with Matter

Once the x-rays are produced at the tube anode, they eventually undergo interactions in their surroundings. CT scanners benefit most from interactions in the detectors and the patient's body, but the photons also interact with collimators and filters, and with the rest of the equipment and with the room structure and furnishings. The following gives a short overview of the important interactions of x-rays with matter.

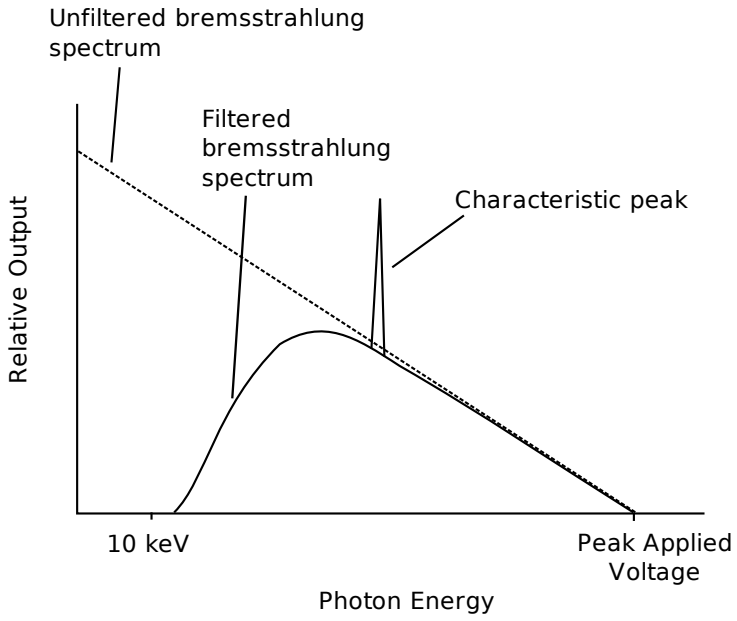

Figure 1.6: The x-ray spectrum from a typical x-ray tube before and after filtering.

There are many ways in which photons interact with matter. Thankfully, only two interactions are important in the range of diagnostic x-rays (below 200 keV): photoelectric absorption and Compton scattering. The photoelectric effect is most significant at low energies, while Compton scattering becomes important with the higher energy x-rays [1]. Before the description of these interactions, two less significant scattering events are mentioned, Thomson and Rayleigh scattering.

Thomson Scattering Thomson scattering is the scattering of photons by free electrons. This follows from classical electromagnetic theory. It is the nearly-elastic scatter of a photon from an electron. This only occurs when $h\nu \ll m_e c^2$ [12]. When this classical assumption fails, Compton's explanation must be invoked. J. J. Thomson, the discoverer of the electron, is given credit for the explanation of this phenomenon. The Thomson cross section per electron is $\sigma_T = \frac{8}{3}\pi r_e^2$, where the classical electron radius is $r_e = e^2(4\pi\epsilon_0 m_e c^2)^{-1}$. While this event is usually not too important practically [13], it has theoretical significance. It is the limit of Compton scattering for zero energy incident photons. It is also the foundation

for calculating the Rayleigh scattering cross section for incoherent photon interactions [1].

Rayleigh Scattering Rayleigh scattering is another scattering event, this time with all of the atomic electrons, not just one. It is a coherent interaction, only important for small photon energy $h\nu$ and large Z materials [12]. Very little energy is transferred and the scattering is forward-peaked [1]. Typically the photon only scatters a few degrees. Thus, these collisions are not important in most applications [13]. At diagnostic energies, Rayleigh scattering events account for less than five percent of interactions [3].

Photoelectric Effect

Turning now to the first of the two important photon interactions, the photoelectric effect is the interaction of a photon with an atom in which the photon is absorbed and an electron is ejected, usually from the innermost (K) shell. This reaction is the dominant interaction below 0.1 MeV in medium- to high-Z materials [12]. The energy of the ejected electron is

$$T = h\nu - \phi,$$

where $h\nu$ is the energy of the incident photon, and ϕ is the energy required to free the electron from the material. This is often equivalent to the electron binding energy but can also include collisional energy losses before the electron escapes [13]. Since the electron shell structure of the atom plays a role in the interaction, the photoelectric cross section is discontinuous [1]. This event gives good contrast for CT imaging [3].

Compton Scattering

The Compton effect was discovered by Arthur H. Compton in 1923. His experiment in 1922 involved K_α x-rays from a molybdenum source with energy 17.4 keV and wavelength 0.714 Å. He measured the wavelength of the x-rays after they had scattered off graphite, discovering that the shift in wavelength $\Delta\lambda$ does not depend on the initial energy of the photons [13]. This is an interaction of a photon with a free electron, such that the photon loses some amount of energy, making the collision inelastic. The relation that describes the energy before (E) and after (E') the collision is [1]

$$E' = \frac{E}{1 + \frac{E}{m_e c^2}(1 - \cos\theta)}.$$

In contrast with Thomson scattering, the momentum of the photon can not be neglected in Compton scattering. Extending the kinematic analysis, Klein and Nishina in 1928 used Dirac's relativistic quantum mechanical electron theory to derive the double differential scattering law for Compton scatter [12]. The formula is

$$\sigma_{KN}(E, \theta_s) = \frac{1}{2} r_e^2 q[1 + q^2 - (1 - \cos^2 \theta_s)],$$

where $q = E'/E$ and θ_s is the scattering angle of the photon [1]. To obtain the cross section for an entire atom, one must multiply by the number of electrons, $\sigma_C = Z\sigma_{KN}$. This is the predominant interaction in tissue at diagnostic energies [3].

The energy and material determine which interaction is more likely. For soft tissue, a 25 keV photon has about equal probability of undergoing a photoelectric absorption or a Compton scatter. Above 25 keV, Compton scatter is more likely, while the photoelectric effect is dominant below 25 keV. For bone, this dividing energy is closer to 50 keV [3].

Half value layer Related to photon interactions is the half value layer measurement. The *half value layer* (HVL) is the thickness of material required to reduce an x-ray beam intensity to one-half its original intensity [3]. This assumes a narrow beam, in which scattered photons do not make it to the detector. The HVL is an indirect quantification of the spectrum of a beam. Since the linear attenuation coefficient decreases with energy, high energy photons penetrate farther than low energy photons. As a beam travels though a filter, its spectrum hardens, and the HVL increases. Since the HVL is simple to measure, it is used frequently in the medical physics community. For a monoenergetic beam, the HVL is

$$\text{HVL} = \frac{\ln 2}{\mu},$$

where μ is the linear attenuation coefficient at the specified beam energy.

1.3 Radiation Dose from CT Scan

Unfortunately, the benefits of CT come at a cost. As a result of the many projections through the body to produce the image, the patient is subjected to much more radiation dose than in a typical x-ray examination. For example, in 2001 CT scans comprised 13 percent of radiological examinations in the United States, but caused 30 percent of

the dose. The situation was even more disproportionate in the UK, where CT scans, making up only 4 percent of the medical imaging procedures, were responsible for 40 percent of the dose from all types of medical imaging [7]. Thus, it is necessary to consider both the benefits and risks of CT scans before undergoing the procedure. It is a problem of weighing the risks involved. While the risk of cancer might be increased slightly with the dose from a CT scan, it is also possible that a poorer image could lead to the radiologist missing an important detail necessary for correct diagnosis [6]. These questions of balancing the benefits with possible risks call for the most detailed, accurate radiation dose information available. This is the motivation for determining the radiation dose spatial distribution to a patient undergoing a CT scan. In order to understand the attempts to determine the dose, a number of key terms are necessary to fully describe the CT scan and the resulting dose. These terms are given in the following section.

1.3.1 Dose Terminology

To fully understand the doses and associated risks from CT scans, one must have broad understanding of a number of diverse fields. Part of the difficulty in grasping the target concepts stems from the diverse backgrounds of individuals involved in the field of radiology. The technicians and radiologist have their own jargon and methods, while engineers and scientists use different terms and tools. Difficulties also arise because some of the risk quantification is not entirely objective. The following terms are some of the basic concepts typically used to describe CT scans.

To quantify the risks from radiation, a number of radiation and dose quantities exist to describe different aspects of the radiation interaction with matter. The first quantity is the photon *scalar flux*. The scalar flux $\phi(\mathbf{r}, E, t)$ is the differential limit of the total number of particles N_p entering a sphere with cross sectional area A per unit time [1]

$$\phi(\mathbf{r}, E, t) = \frac{d^2 N_p}{dA\, dt}$$

at position $\mathbf{r}$, with energy E, and time t. The photon fluence $\Phi(\mathbf{r}, E, t)$ is the total scalar flux multiplied by the total time of exposure.

The next quantity is *exposure*. The exposure X is the absolute value of the ion charge of one sign in air produced by all electrons except for bremsstrahlung per unit mass of air. The exposure is only valid in air. The traditional unit of exposure is the röntgen

(R), which is defined as 2.58×10^{-4} coulombs per kilogram air. If the photon flux is known, a simple formula exists to calculate the exposure. The exposure response function

$$\mathcal{R}_X(E) = 1.835 \times 10^{-8} E \left(\frac{\mu_{en}(E)}{\rho} \right)_{air} \qquad [\text{R cm}^2], \tag{1.3}$$

with E in MeV and μ_{en}/ρ in cm^2/g, is folded with the scalar flux to obtain the exposure [1]

$$X = \int_E dE\, \mathcal{R}_X(E)\Phi(E). \tag{1.4}$$

The mass attenuation coefficient is tabulated by Shultis and Faw and is included in Appendix A. The exposure is commonly used because it is easy to measure with ionization chamber radiation detectors [14].

The *absorbed dose* is one of the most fundamental and objective of the dose quantities. Loosely, the absorbed dose is defined as the energy imparted by radiation to a given unit mass of the target [1]. The unit of measure of absorbed dose is the gray, abbreviated Gy. One gray is equivalent to one joule per kilogram. The traditional unit of rad (*r*adiation *a*bsorbed *d*ose) is equal to 0.01 Gy. The röntgen-to-rad conversion factor is roughly 1 for soft tissue at diagnostic energies.

A related quantity is the *k*inetic *e*nergy *r*eleased in *ma*tter, *kerma*. Kerma includes all the energy imparted to ionize particles. Some of this energy may be carried away in the form of bremsstrahlung, but this is irrelevant for kerma [3].

The *equivalent dose* or *dose equivalent* is defined as the product of the absorbed dose and a radiation weighting factor (previously known as quality factor). The unit of equivalent dose is the sievert, abbreviated Sv. The traditional unit of rem is equal to 0.01 Sv. This is intended as an adequate measure of the health risks of radiation. For diagnostic radiation, the weighting factor is one. For heavy charged particles, the weighting factor is greater than one [3].

A less fundamental parameter, but one that corresponds more closely to risk is the effective dose. *Effective dose* is a good measure of the potential risks from radiation when the radiation is well below the threshold for deterministic events. It provides a whole body dose that is equivalent in risk to the individual from a radiation dose to specific tissue or an organ of the body. Effective dose, E, is defined by Publication 60 of the International Commission on Radiological Protection (ICRP). The effective dose is the equivalent dose to specific tissue or a specific organ multiplied by a weighting factor for that tissue or organ.

Table 1.1: Typical effective dose caused by various medical and other sources [6].

Event	Dose (mSv)
CT scan	6
Chest x-ray	0.02-0.05
Barium enema	3-7
Nuclear medicine procedure	5
Background radiation	3/yr
Limit for radiological worker	50/yr
Limit for general public	1/yr

The unit for effective dose is the sievert, Sv. A similar quantity, the *effective dose equivalent*, H_E, is outlined in ICRP 26. Both the effective dose and effective dose equivalent are similar in nature. They are both based on relative weighting scales to quantify the risk of radiation dose to specific tissue or organs. The difference lies in the values of these weighting factors. The weighting factors are chosen so that the effective dose is proportional to the stochastic risks of cancer induction and genetic defects [15]. It should be mentioned that often *dose* is used in a generic sense, without specific reference to either absorbed dose or effective dose.

One final quantity applies specifically to CT. The *Computed Tomography Dose Index* (CTDI) characterizes radiation output. It is the linear integration of the absorbed dose (in air) along the axial direction of the scanner for a single slice, divided by the nominal slice width. This is measured with TLD's suspended along the scanner axis [16].

1.3.2 Typical Dose and Associated Risks

It is useful to examine the typical doses imparted during medical imaging procedures. This establishes a basis to evaluate the relative risks associated with certain procedures. The typical effective dose for a number of medical procedures as well as other events for reference are provided in Table 1.1. It is clear that CT scans impart much greater dose than chest x-rays, by a factor of one hundred or more. The effective dose from a CT scan is of the same order of magnitude as the background dose received by the average American per year.

For our purposes, abdominal scans are of special interest. Some details about

abdominal scans follow. In an abdominal CT scan with the applied potential of 120 kVp, the effective dose varies significantly for adults *vs* children. For children (less than 10 years of age), the effective dose is 6.1 ± 1.4 mSv, for young adults aged 11 to 18, the dose is 4.4 ± 1.0 mSv, and for adults over 18, it is 3.9 ± 1.1 mSv. Thus, with the same scan parameters, children receive a fifty-percent-higher effective dose. These values are comparable to the doses received from nuclear medicine ($2 - 10$ mSv), barium enema examination ($3 - 7$ mSv), and excretory urography ($2.5 - 5.0$ mSv). They are much higher than traditional x-ray procedures ($0.02 - 0.05$ mSv for a chest x-ray and $0.5 - 1.5$ mSv for the abdomen) [15]. In another survery, the National Evaluation of X-Ray Trends, the median dose equivalent for an abdomen and pelvis CT scan was 13 mSv in the year 2000 [8].

Risks

Doses from CT scans are well below required thresholds to cause deterministic effects such as skin inflammation and loss of hair. *Deterministic effects* occur predictably at high levels of radiation. For CT scans, risks are limited to stochastic effects, which include carcinogenesis and the introduction of genetic defects [6]. *Stochastic effects* are those events which happen according to a certain probability, often only manifesting themselves years later after the dose is incurred. The effective dose is the best quantified correlation between the amount of radiation received and the resulting risk of experiencing one of the stochastic events [6].

Risks to Fetus

The radiation risk to humans is greatest in the early stages of development. This is why the determination of uterine, conceptus, and fetal dose is so common and important. This is the limiting case—the most sensitive period in the development of a human embryo. A number of experimental and computational projects have been conducted to determine the dose to a fetus for various medical radiography procedures.

Felmlee Study In a study by Felmlee *et al.*, a humanoid phantom, the Rando phantom, was used to examine the radiation dose to a fetus. Four different CT scan machines were used at a variety of tube potentials. The fetus was estimated to be located in slice 32, one-quarter of the body thickness below the anterior, which was a depth of 9 cm. The doses

measured were in the range of 0.06 mGy to 33 mGy, depending on the location of the scan. Care was taken to isolate the various paths of transport of the radiation, i.e. uncollided flux and scatter from the gantry or table. To evaluate gantry scatter and tube leakage, a 0.5-mm lead-equivalent rubber photon shield was inserted between the scanned slice and the fetus slice. This eliminated nearly all of the internally scattered x-rays from reaching the fetus, giving a good estimate of the magnitude of external scattering. The external scattering source becomes a very significant portion of the total flux in regions away from the direct beam. For example, with the scan slice at a 40 cm offset from the fetus slice, the x-ray tube leakage and gantry scatter contributes 14 percent of the dose, internal scattering is responsible for 56 percent, and the other 30 percent comes from scattering from the room. However, the dose at such a large offset of the fetus from the useful beam is usually not significant. For 40 cm, the dose is two to three orders of magnitude less than the dose in the direct beam [17].

Using their presented empirical methods along with the data generated in this experiment, the authors achieve a general agreement of ± 15 percent with experimental measurements taken with a variety of CT machines and scan parameters, from direct irradiation to a 40 cm offset. Including the individuals' varying body sizes and shapes, the agreement is within 20 percent. They also concluded that 30 cm and greater offset yielded negligible dose to the fetus [17]. Based on these results, it would be safe for a pregnant patient to undergo a head CT scan.

Osei Study In a retrospective study of 50 pregnant women by Osei *et al.*, most of the women were not aware of their pregnancy until after the radiological procedure, not specifically CT scans [18]. In the study, the range of doses was estimated to be between 0.01 μGy and 117 mGy. The gestation time when the medical imaging took place was between 2-24 weeks. Out of the 50 participants, only two received doses greater than 100 mGy, while most (64 percent) received less than 10 mGy. All doses were well below the threshold of 390 mGy for death and malformation, except for two at 114 mGy and 117 mGy, which begin to approach the threshold. The authors estimate that even with the maximum dose observed in the study, the maximum loss of IQ points for the child would be four. This is too low to discern on an individual basis. All of the risks from radiation were smaller than naturally present risks [18].

Dietrich Study This is the experiment of primary interest because it is the basis of our computational model. This study was performed at the Hershey Medical Center using a similar Rando phantom as Felmlee (see Figure 1.7). Using lithium-fluoride thermoluminescent dosimeters (TLD), the absorbed dose was measured at the phantom's surface as well as at select points in the interior. Slice 31, position C6, was estimated to best approximate the location of a conceptus within the uterus. The location of this slice is visible in Figure 1.8. The scans were over the abdomen and pelvis of the phantom. Both axial and helical scans were performed. For the axial scan, the applied potential was 120 kVp, the current was 200 mA, the scan slices were 8 mm in width, which is roughly half the width used in the experiments for this project. Each revolution took one second. Twenty-six total slices were imaged. The maximum surface dose was measured to be 60.7 mGy and the average was 45.3 mGy. At the conceptus location, the dose was 33.7 mGy [19]. In slices outside of the direct beam, the logarithm of the dose decreased linearly with the normal distance from the edge of the beam.

For the helical scan, the applied potential was 120 kVp, the current was 150 mA, the scan slices were 5 mm in width, and each revolution took one second. The maximum surface dose was 22.9 mGy and the average was 18.4 mGy. At the conceptus location, a 14.9 mGy dose was reportedly measured. Outside of the beam, the same rate of decrease was observed as for the axial scan. In both cases, the surface dose was greater than the uterine dose. The results agree well with a simplified method of determining dose [7]. According to this method, the dose from a CT scan is nearly uniform at the surface. In the head, it is also close to uniform. In the trunk, there is greater variation. The dose at the center is roughly half of that at the surface. For both the axial and helical scan, the conceptus dose is roughly half of the surface dose.

One other conclusion from the experiment was that the conceptus dose was less than the 50 mGy limit that might lead to consideration of an abortion. Additionally, the authors determined that for a location at least 13 cm from the direct irradiation by the x-ray beam, the dose is vastly reduced and is insignificant.[19]

Other General Pregnancy Concerns Pregnancy complicates many of the judgements which a radiologist must make. The question of whether a CT scan should be performed is complicated by the need to consider the risks to both the mother and the child—of having

Figure 1.7: The Rando phantom posterior in its holding brace.

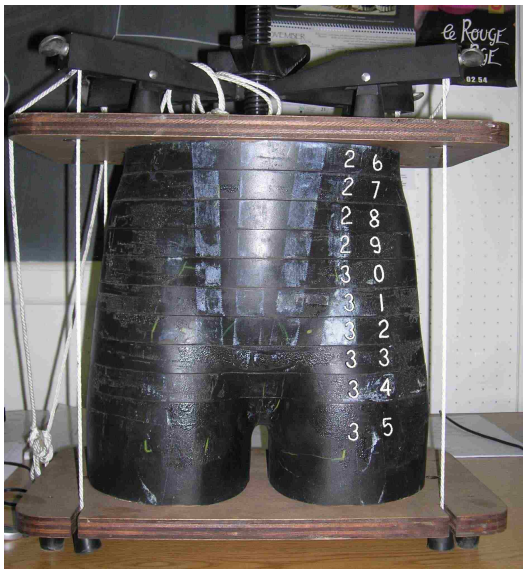

Figure 1.8: The Rando phantom anterior in its holding brace. The slice numbers are colored for better visibility.

or not having the procedure. It should be remembered that the well being of the mother is also a benefit to the child. Guidelines exist which aim to limit the dose a fetus might receive. High dose procedures should only be performed in the early portion of the menstrual cycle for those women who could potentially be pregnant. However, this guideline is not always followed [18].

During pregnancy, certain stages of development of the fetus are more sensitive to radiation than others. The 8-15 week gestation period is the most sensitive time. During this period, the risk of decreased mental capacity is estimated as a loss of 30 IQ points/Gy. The risk of inducing genetic hereditary effects is about 2.4×10^{-2} /Gy, and the risk of fatal cancer before the age of 15 is 3.0×10^{-2} /Gy [18]. Specifically, the gestation period from 8 to 15 weeks has the highest risk of severe mental retardation when the fetus is exposed to radiation. The period from 8-15 weeks has a risk four times greater than the gestation period from 16-25. No mental retardation was observed in children born to mothers who were exposed to radiation fewer than 8 weeks or greater than 25 weeks in the gestation period. This conclusion was reached from the study of the survivors of the atomic bomb in Japan [20]. This differing sensitivity and risk can be explained in terms of the stages of fetus development. The 8 to 15 week range is the period of most rapid neuron proliferation. Thus, radiation has a higher chance of inducing neuron irregularities. During this time period, the frequency of retardation is proportional to the fetal effective dose [20].

1.3.3 Causes of the Dose

The dose received from a certain CT scan is dependent on many factors. Understanding what these factors are and how they may affect the dose is the first step to minimizing the dose. For example, in an abdomen scan, the absorbed dose to the patient varies by a factor of 10 to 40 depending on the particular machine, procedure details, and other variations. When comparing dose due to only a single CT machine model, the dose can still vary 5 to 20 times [16].

The first set of factors are directly related to the x-ray beam tube. The three main options in operating the tube, the applied voltage, the current, and the total procedure time all have a direct effect on the dose. The applied voltage, or potential, affects the energy of the photon beam. The potential is normally maintained at a constant level. In the experiments of Ravenel, the tube potential was maintained at a peak kilovoltage of 120 kVp for all

scans [6]. In the Felmlee study, the potentials tested were 100, 120, 130, and 140 kVp [17]. These differences have a strong impact on the dose. An increase in the applied potential from 120 kVp to 140 kVp increases the dose 30 to 40 percent [7]. Also, the current and time are proportional to the dose. Their combined effect is measured in milliampere·seconds (mA·s).

Not only do these factors influence the dose, but the model type of the CT machine and the age of the x-ray tube play a major role as well. The radiation output of an x-ray tube can vary by up to 30 percent over the lifetime of the tube. With an assumption of a 1 mm to 2 mm variation in the width of the collimated beam, this translates into a 40 to 50 percent error in the dose calculation [17]. The dose also differs significantly between different CT machine models. The effective dose equivalent (H_E) varies by a factor of three for comparable image qualities across models. The discrepancies are caused by differences in the distance between the axis of rotation and the x-ray focus point, the potential applied to the x-ray tube, and the amount and type of beam filtration [16]. Additionally, the dose is dependent on the number of slices imaged, the width of the slices, the use of contrast medium for additional scans, and machine exposure settings [7, 16].

1.4 Computational Models of Dose

Since experiments with CT scanners are costly and have many unknowns, it is profitable to develop computational methods to determine the dose distribution through the patient. The main challenge is calculating the energy dependent photon flux distribution. With the flux known, the various dose quantities are much simpler to compute. The problem of determining the flux distribution in matter is the realm of radiation transport. For neutral particles (photons and neutrons), the governing equation is the linearized Boltzmann equation [21]

$$\frac{1}{v}\frac{\partial \psi}{\partial t} + \mathbf{\Omega}\cdot\boldsymbol{\nabla}\psi + \sigma(\mathbf{r},E)\psi(\mathbf{r},\mathbf{\Omega},E,t) = \int dE' \int d\Omega' \sigma_s(\mathbf{r},E'\rightarrow E,\mathbf{\Omega}'\cdot\mathbf{\Omega})\psi(\mathbf{r},\mathbf{\Omega}',E',t) + q(\mathbf{r},\mathbf{\Omega}',E',t), \quad (1.5)$$

where

$\mathbf{r}$ = position vector,
$\mathbf{\Omega}$ = direction unit vector along the particle's path,
E = particle energy,
t = time,
ψ = angular flux, the component of the scalar flux traveling in a particular direction, such that $\phi = \int d\Omega\, \psi$,
v = particle speed,
$\sigma(\mathbf{r}, E)$ = total macroscopic cross section, the probability of any interaction per unit path length traveled,
$\sigma_s(\mathbf{r}, E' \rightarrow E, \mathbf{\Omega}' \cdot \mathbf{\Omega})$ = double differential scattering cross section, the probability that a particle with energy E' and direction $\mathbf{\Omega}'$ will scatter to an energy E and direction $\mathbf{\Omega}$,
q = external particle source.

This equation is defined over the spatial region V with boundary ∂V. Incoming angular flux boundary conditions must be specified, such that

$$\psi(\mathbf{r}_s, \mathbf{\Omega}, E, t) = \psi_0(\mathbf{r}_s, \mathbf{\Omega}, E, t) \quad \text{for} \quad \mathbf{\Omega} \cdot \mathbf{n} < 0,$$

where $\mathbf{r}_s \in \partial V$ and $\mathbf{n}$ is the unit normal to the surface ∂V at $\mathbf{r}_s$.

In diagnostic medical physics problems, a time independent form of the equation is usually sufficient. It is possible to model the x-ray beam as either an external source q or an appropriate boundary condition, but usually one of these two is set to zero. Even with these simplifications, the Boltzmann equation requires numerical solutions for all but the simplest of configurations. A variety of computational methods have been developed to solve this equation, with varying levels of fidelity, complexity, and speed. The following sections detail the primary algorithms used in medical physics. First, simplistic, approximate methods are described. Then two high-fidelity methods are presented, Monte Carlo methods and deterministic methods. In addition to the short theoretical descriptions, relevant work in medical physics and specifically concerning CT simulations is mentioned.

1.4.1 Simple Algorithms

The radiation transport problem of diagnostic medical physics is a rather specialized case. Thus a large number of approximate methods have been developed to calculate the patient dose. Some of the factors which make this possible are the low photon energies, the collimation of the beam, and the similarity of patients. As an example, in many ways,

a tissue-equivalent water phantom gives satisfactory results, making the exact geometrical details of the patient unimportant.

While these methods have their foundations in theory, they often rely heavily on empirically-determined constants and fudge factors to obtain accurate results. Larsen outlines a number of such approximations for radiation oncology, which makes use of higher energy photons than CT, in addition to electrons [22]. Many of the methods are based on Fermi's *pencil beam approximation*. The pencil beam approximation assumes that the scattering is mostly through small angles, so that the beam stays a beam. With this approximation, the beam slowly widens as it travels through a medium. The spatial shape of the beam is a Gaussian in the transverse directions. Using this form, experiments are conducted to find appropriate fitting parameters. This can be an accurate method, although it requires the clinical situation be similar to the experimental setup. As the clinical application deviates from the original procedure, the calculated results grow more suspect.

There are many other methods with higher accuracy. The dose spread arrays approach builds a library of radiation events using an initial Monte Carlo simulation [22]. Then, when a dose calculation is needed, the library data is selectively combined using convolution integrals. This ends up being a quick and accurate way to calculate dose. A similar method was published by Kalender *et al.* in 1999 for a program capable of running on a desktop computer [23]. This program uses an analytic approach to calculate the uncollided flux and Monte Carlo-generated data libraries for the scattered radiation to calculate organ doses for both axial and spiral CT. This program generally achieves results within five percent of other published data.

Geometrical considerations In addition to the computational methods available, there are also numerous techniques to reduce the complexity of the radiation model. In the area of geometrical simplifications, modeling the human torso or head as a cylinder of water is a common practice. Ware demonstrates this method [15]. The radius of this water cylinder is based on the estimates of the trunk's semi-major axis a and semi-minor axis b in the relation:

$$r = \left[a \cdot b \left(\frac{\rho}{\rho_w} \right) \right]^{1/2},$$

where ρ_w is the water density, and ρ is the body density. The ratio of densities accounts for variation in the body or tissue density. For example, the trunk density of newborns is

close to 0.995 g/cm^3, but it increases to 1.018 g/cm^3 for adults. In their experiment, the sample of 36 adults had an average mass of 74.8 ± 19.4 kg. The equivalent water cylinder radius was 14.5 ± 2.2 cm [15].

The authors raise an interesting point concerning this water phantom cylinder approximation. Their experiment yielded an average water diameter of 29 cm. The typical acrylic cylindrical phantom used for dose measurements is 32 cm in diameter. When this is corrected for the density of acrylic ($\rho = 1.19$ g/cm^3), the average diameter of water in the phantom is close to 35 cm. This means that the acrylic phantom will tend to under predict dose because it is significantly larger than the average person. As these phantoms are generally only useful for rough estimates, this difference is not perceived as a serious problem, but it is important to at least recognize the discrepancy [15].

In the problem at hand of calculating conceptus dose, the uterine dose becomes an important intermediate calculation. The embryo and fetal dose can be estimated from the non-pregnant uterine dose. When the uterus becomes enlarged during pregnancy, the tabulated doses for the uterine dose must be adjusted. Using the non-pregnant uterine dose to predict the dose to a pregnant uterus will tend to over predict the dose, although this may not be significant [18].

1.4.2 Monte Carlo Methods

Monte Carlo methods rely on modeling the natural phenomena comprising the transport process with many individual particles. The observable results, for example the dose, are obtained by computing mean, or expected values of the contribution to the specific observable from all the modeled particles. In this way, Monte Carlo is analogous to the physical situation which Equation (1.5) describes [21]. In the following work MCNP5 is the Monte Carlo code employed. MCNP5, Monte Carlo Nth Particle code Version 5, is a full-featured particle transport simulation code implementing stochastic methods developed at Los Alamos National Laboratory [24].

In Monte Carlo, a *history* is the individual unit of simulation which is repeated to obtain averages. In the case of particle transport, a history is the lifetime of an individual particle and all its progeny, from its birth at a source, through interactions, ending when the particle and all its daughter particles are absorbed or terminally leave the region of interest. The details of each lifetime are based on the physics of the situation and on chance. For

each event in a particle's life, such as distance of flight to the next collision or scattering angle, a physical probability distribution is known. This requires data describing a great number of possible interactions. In particle transport applications, this data is contained in large nuclear cross-section libraries. Thankfully, for common usage, MCNP5 is equipped with libraries of such data that provide it access to this information with minimal user intervention, making the computation transparent and less prone to error.

While the known probability distributions seek to make the simulation correspond accurately to reality, chance and randomness are required to ensure that the histories uniformly represent the multitude of possible combinations of events in a particle's life. In a digital computer simulation, this randomness is introduced by a pseudo random number generating algorithm. The mathematics behind these algorithms make this one of the most abstract elements of Monte Carlo methods, but the results of the generator are simple. The pseudo-random number generator produces a repeatable sequence of uncorrelated real numbers with a uniform distribution over the unit interval. Also significantly, the sequence is repeatable given the starting value, or *seed*, in contrast to truly random sequences that are not repeatable. The ability to repeat the sequence is essential for testing and verifying results, and debugging the code employing the pseudo-random numbers. With a sequence of pseudo-random numbers and known probability distributions describing the various events a particle might encounter, it is possible to construct a history.

By recording certain events encountered within each history, the program reports averages of selected quantities, for example particle flux and energy deposition, depending on the user's instructions. The recorded quantities are called *tallies*, and come in a variety of flavors. In MCNP, tallies are specified in the input file by the user before the program run, and the computed result is reported in the output file as a normalized value per source particle. Tallies are generally associated with cell volumes or surfaces in the problem domain. For example, MCNP5 has flux tallies for surfaces and volumes. The surface flux is simple to compute; the flux is essentially the number of particles which cross the surface in any direction normalized by the surface area and divided by the direction cosine of incident particles. For the volume flux, the calculation is slightly more complicated. Based on the mathematical equality that the flux can be computed as the ratio of the total particle path lengths to the cell volume as the volume approaches zero, MCNP maintains a record of the total distance traveled by the particles in a specified cell. This allows for an estimate of the

flux in that cell by taking the ratio of the computed total distance to the cell's volume.

Just as real experiments are subject to experimental uncertainties, Monte Carlo is always limited by statistical uncertainties. The magnitude of the uncertainty typically decreases with increasing number of histories. MCNP5 estimates these uncertainties for all the tallies it produces per the user's specifications. It has ten measures of the statistical validity of a result, the most significant being the standard deviation given as a relative error. For most purposes, this error should fall below five percent to have reasonable confidence in a tally's result. The standard deviation of a tally about the true mean value varies inversely with the square root of the number of histories. Thus, for a one-hundred fold increase in the number of histories, the uncertainties will only decrease by a factor of ten. This relatively slow rate of convergence is the major disadvantage of Monte Carlo methods. A large number of tallies requires much computing resources. To combat this limitation, biasing techniques have been developed to speed the computation. Biasing usually involves the assignment of high interest and low interest regions in *phase* space, comprised of physical space and velocity, or equivalently energy, angle, and space. Particles, through a variety of means, are encouraged to enter the regions of greater interest. While the concepts of analog Monte Carlo are intuitive, the non-analog techniques designed to reduce variance introduce many complications. For this reason, the use of biasing techniques risks incorrect results when employed by an unexperienced user. Improperly applied, they can create high confidence in a result that is incorrect.

Even with biasing methods, Monte Carlo methods are still impractical for clinical applications. In 1997, when Larsen published his tutorial on radiation transport in oncology [22], it was generally accepted that Monte Carlo methods were roughly 1000 times too expensive. For the technology to be widely accepted, the simulation time must be around 10 minutes, a difficult goal for MC methods. For one-time verification calculations, this long run time is of little concern, but for production runs this burden can be debilitating.

However, the high computational expense is balanced by a number of benefits. The advantage of MCNP is its ability to model physical processes without being forced to use assumptions or make the abstractions required by deterministic methods. The major example of this is the superior method by which MCNP5 treats energy dependence. In deterministic methods, particles of similar energies are lumped into groups, with corresponding average cross sections for these groups. While much experience in developing

these multi-group cross sections has led to success for certain problems, the cross section sets have limited applicability outside their originally intended application. Developing the multi-group cross sections is a non-trivial task because the spectrum used in collapsing the detailed energy dependence of the cross sections over groups is highly problem dependent. Thankfully, MCNP5 circumvents this problem. Because each history is evaluated individually following the progress of its sequence of events one collision at a time in continuous energy dependence, no lumping into energy groups is necessary. The energy dependence of the cross sections can be as fine as the data libraries allow, with interpolation (typically linear) between points.

MCNP5 is also capable of modeling secondary electron transport in a natural way. Deterministic methods require altering the cross sections to account for the transport of charged particles in an efficient manner, and lack a simple means to track the movement of the charged particles after their creation. This fact follows from the fact that charged particles interact with one another and with the host medium via continuum Coulombic forces, resulting in infinitesimal mean free path length. None of these problems afflict MCNP5.

Existing Monte Carlo CT Models

The Monte Carlo method is the most active area of research for computing dose estimates in CT scans [25, 26, 27, 28]. The review paper "Current status and new horizons in Monte Carlo simulation of X-ray CT scanners" provides an overview of the recent work in the field [29]. The ability of MC codes to accurately estimate internal doses has been validated using the production codes MCNP [26] and EGS4 [30].

The MCNP paper [26] is especially relevant since this is the same program used in this thesis. For the study, the authors based their model on a General Electric Medical Systems scanner which produced slice thicknesses of 1, 3, 5, 7, and 10 mm. The tube potential could be set to 80, 100, 120, and 140 kVp. The machine has both axial and spiral scan modes. There is internal filtration as well as external filtration from the bowtie filters. Two bowtie filters are provided, one sized for the head and the other for the body. The fan beam angle is 49°. The focal spot (the location on the anode from which the x-rays are emitted) to the isocenter is 63 cm, and the focal spot to detector distance is 110 cm. The authors implemented a model of the scanner in MCNP4B. They modified the

source code to specify exactly the source for both axial and spiral scanning protocols. For the x-ray spectrum, they used the TASMIP code by Boone and Seibert since they were unable to measure the spectrum directly [31]. The internal filtration was accounted for in the calculation of the spectrum, and was not simulated in MCNP. The bowtie external filtration was modeled by reducing the weight of the particles according to the total path length through the bowtie filter. The computational model was to be validated using the CTDI head and body phantoms, acrylic glass cylinders 15 cm in length and 16 and 32 cm in diameter, respectively. The CTDI phantoms were scanned in the GE machine, and exposure measurements were taken with a ion chamber. In addition to the CTDI phantom, the authors also simulate the MIRD-V anthropomorphic phantom and a patient-specific geometry. The MIRD-V is a rough approximation of a human with the organs represented as simple geometric shapes. The patient-specific data is from CT scans of a particular person.

The paper discusses two measurements conducted. The first was the in air exposure for purposes of normalizing the model source. The second measurement was of the dose in the center and peripheral location of the CTDI head and body phantoms. Interestingly, the scanner table was found to influence the dose at the bottom of the phantom, so the table was added to the model. In the end, the authors report 8% agreement in the measured and computed doses at the center and 6% at the periphery over all tube potentials and slice thicknesses. For the MIRD phantom, nearly all organs were within 10% of the accepted values for the axial scan. Only a few changes were observed for the spiral scan. Finally, the authors were able to simulate the patient data successfully, obtaining dose distributions for the patient's organs.

Many subsequent studies have examined various scan parameters and design choices to quantify the effect on the patient dose. Since there are many parameters to vary, including scan time, tube current and potential, scan pitch, and slice thickness, MC simulations are useful in examining the effects of the variations in these parameters, in an effort to reduce dose. In addition to dosimetric studies, MC is also employed in the simulation of the entire CT device [32]. In addition to modeling the source and the patient, these simulations include the detector elements as well. Such simulations can aid in the tuning of reconstruction algorithms to reduce artifacts caused by scattered radiation.

1.4.3 Deterministic Methods

Deterministic radiation transport methods are less intuitive than MC simulations. The solution methods are more akin to numerical differential equation methods used in applied math such as finite difference and finite element methods. A full description of representative deterministic methods is available in Lewis and Miller [21]. In broad terms, each independent variable of the angular flux in Equation (1.5) is discretized. The energy discretization is accomplished by the use of energy groups. Then an energy independent version of the equation can be solved for each group. Particles may scatter from one group to another, depending on the cross sections. Generating the cross sections proves to be one of the most difficult tasks in using these methods. The method to generate this data will be discussed later. In the discrete ordinates approximation of the transport equation, the angle variable is discretized by solving the equation over a set of discrete ordinates, called a quadrature set. Finally, the spatial variables are split into a mesh of discrete points.

Existing deterministic models

In contrast with Monte Carlo methods, full deterministic models are much less common in medical physics. Note that many deterministic algorithms are employed for dose calculations, but almost always these are grossly approximate methods such as the pencil beam approach described above. Although there is not much existing work, some research efforts have been made in preliminary application of deterministic methods to radiography and radiotherapy. This is often because these methods are traditionally more computationally efficient [33]. One paper describes an integral transport equation-based deterministic computer program for the computation of CT dose [34]. The program uses a first collision source iterative approach. Since the photons scatter only a few times at most, this method converges quickly. Since the program takes the geometrical input from CT data, the number of computational cells is large. Thus, the memory requirements are greater than a single desktop machine can accommodate. Therefore, the program also implements a parallel algorithm using spatial domain decomposition. For the sample calculation of a head scan on the Visible Human dataset, the problem used four million voxels, 1 mm by 1 mm by 2 mm. The uncollided flux was calculated in one keV energy bins, while the scattered fluxes were put into five groups. On a 64-node high performance cluster, the

execution time was 4 minutes for the uncollided flux and 120 minutes for the scattered flux. Although the paper demonstrated the potential of deterministic methods, in this case the required compute power is even greater than that required for a MC simulation.

Looking beyond CT models, there are additional medical physics applications of deterministic codes. In one model of external beam therapy, the deterministic code TORT achieved good agreement with a Monte Carlo code named EGSnrc for parallelepiped-shaped cells (called *voxels*) within the beam. Poor results were obtained for cells on the beam edge, where a sharp flux gradient existed [33]. The commercial finite-element code Attila has been benchmarked against MC methods for radiotherapy applications, both for a brachytherapy source and an external beam. For the brachytherapy problem, the difference in the calculated doses was less than 2% for the majority of the space, although some errors up to 5% were observed. The MC simulation took 990 minutes, while the Attila calculation lasted 20 minutes. For the external beam, the largest observed error was 2.2%.

Much of the reported work has been in the area of Boron Neutron Capture Therapy. Boron Neutron Capture Therapy (BNCT) is an especially challenging computational undertaking, because of the multiple modes of dose deposition. Each cause has a different relative biological effectiveness [35]. A number of papers report the use of deterministic code packages for treatment planning applications for BNCT. Deterministic methods avoid the statistical errors inherent in Monte Carlo that cause serious problems in regions of low flux but incur truncation errors due to discretization and convergence errors due to the iterative solution strategy typically adopted. In addition, small changes in the flux computed by deterministic methods resulting from varying input parameters are not blurred by the statistical errors of Monte Carlo. For the BNCT model, the requirements for the method employed in computing the dose were that it completely treat all necessary particle transport phenomena, that it have flexibility in defining the source beam shape and angular distribution, and that it have an accurate meshing structure [36].

Specifically, the discrete ordinates, commonly referred to as S_N, method is applied to phantom experiments. In one study by Nigg *et al.*, a canine head phantom was irradiated by an epithermal neutron beam at the Brookhaven medical research reactor. The phantom geometry was modeled by a mesh of 1 cm^3 voxels. The material assignment for all voxels was homogeneous. With a mesh size of $32 \times 16 \times 22$ and 96 discrete directions, agreement with the experimental results was achieved within 15%. The calculation took one order of magnitude

longer than comparable Monte Carlo (MC) codes. In this case, the deterministic method was useful in verifying the Monte Carlo code. It also provided spatial flux distributions, which neither MC nor experimental methods were capable of producing [35].

In work done by Ingersoll *et al.*, a human leg undergoing BNCT was modeled in TORT with a disk source. The results from a MC calculation agreed to within 10 percent of the TORT answers. To achieve this level of accuracy, 10^7 histories were run in MCNP. For the TORT model, a cross section library with 47 neutron groups and 20 photon groups with a P_5 Legendre expansion of the scattering anisotropy was used, while a S_{12} angular quadrature was employed to discretize the angular independent variable. TORT ran three times faster than the MCNP model. The authors concluded that TORT, and other deterministic models in general, are well suited to solve problems on voxel-based anatomical models [37].

Chapter 2

Experimental Stage

The goal of the experimental stage of this work is the acquisition of high-quality data for the irradiation of phantoms in a CT machine. Diverse radiation detection instrumentation should be employed to quantify uncertainty in the dose measurements. Since dose values for the Rando phantom are available from the Dietrich study [19], the focus is on gathering data for the geometrically simpler FDA body phantom.

These experiments were conducted at the Penn State Hershey Medical Center (Hershey) using the equipment available in the Department of Radiology and the Division of Health Physics. The experiments were performed on January 3, 2008 by Steven King, Michael Erdman, other Hershey support staff, and Joshua Hykes. Since the machines are in high demand, the data collection was performed as efficiently and quickly as possible. The machine was available for testing for approximately thirty minutes.

The experiment used a Siemens Somaton Sensation 16 CT scanner. An FDA CTDI body phantom (Nuclear Associates 76-414 CT body dose phantom, Carle Place, NY) was utilized [38]. This is a cylindrical acrylic phantom, 15 cm tall and 32 cm in diameter with a drilled center hole and four peripheral holes located at 12, 3, 6 and 9 o'clock, in accordance with FDA standards [39]. The holes have an inside diameter of 1.31 cm. The CT machine scan parameters used for all tests were 120 kVP, 200 mA, 1:1 pitch helical scanning, 16 slices at 1.5 mm per slice.

During the experiments, two instruments took each reading. The first was a 10 cm pencil ion chamber (Radcal MDH 1515 with 10X6-3CT CT chamber; Radcal Corporation, Monrovia, CA) that measured exposure. The second was an optically stimulated

luminescence (OSL) dosimeter designed for CT (Landauer, Inc., Glenwood, IL). This is a thin strip of an aluminum oxide crystal that becomes excited in the presence of ionizing radiation. When the crystal is exposed to light of a certain wavelength, the excited electrons can recombine with electron holes, producing light. The advantage of this process over thermoluminescence dosimetry is that a small portion of the crystal can be read at a time, thus endowing the measured dose with a spatial profile. It is a simple matter to shine a thin laser onto a small portion of the material, while heating only a specific location is less practical. Thus, it is possible to achieve high spatial resolution. In the report from Landauer, the resolution was 0.05 mm. In contrast with the ion chamber, the OSL dosimeters measure total dose.

In air test The first test was an in-air measurement of the exposure using an ion chamber and an OSL dosimeter. First, the ion chamber was placed at the isocenter of the CT opening. The entire length of the probe was scanned, so that the exposure accumulated over the 10 cm length. The total scan time was 5.59 seconds and the total travel length was 139 mm. In air measurements using the MDH pencil chamber at the isocenter averaged 4.11 roentgen (R), with the individual tests yielding 4.10, 4.11, and 4.11 R.

This procedure was replicated using the OSL dosimeter. The OSL dosimeter was placed in air on the patient couch and positioned isocenter within the CT opening. The OSL measured a total integrated dose along the dosimeter as 3337.2 mGy (333.7 rad). The CTDI_{100} was

$$\mathrm{CTDI}_{100} = \frac{333724 \text{ mrad}}{1.5 \text{ mm/slice} \cdot 16 \text{ slices}} = 139.05 \text{ mGy}(13.9 \text{ rad}).$$

The report from Landauer on these measurements is given in Figure $B.1$.

X-ray beam hardening test It is important to characterize the beam hardening, which relates to the amount of filtration through which the beam travels before it enters the patient. To estimate the beam hardness, the exposure was measured with and without an aluminum sheath. The test configuration was similar to the in-air test. Without the aluminum, the ion chamber gave readings of 3.33 R and 3.33 R in two consecutive tests. Then a 3.2 mm aluminum shell was placed around the ion chamber. With this in place, the exposure was reduced to 2.98 R and 2.96 R. These results will be discussed in more

detail, but note here that they led to inconclusive results for the half-value layer (HVL) of the beam. The half-value layer is the quantity of material necessary to reduce the beam to half its original strength. The HVL is a simple method to measure beam hardening. Thus, a dedicated instrument was used to measure the HVL. We measured the HVL with the Barracuda probe (RTI Electronics, Fairfield, NJ). It has several thicknesses of aluminum as a step wedge and does an automatic HVL calculation. With this instrument, we measured an HVL of 8.8 mm aluminum.

FDA phantom test Finally, with the preparatory experiments complete, we conducted the scan of the FDA phantom. First, the ion chamber was placed in the phantom's center hole and in one of the peripheral holes and the radiation was accumulated over the 10 cm length. The scan went an extra 3 mm beyond each edge of the 15 cm long phantom to image the entire phantom uniformly. Since this was a slightly longer scan, the time and length were also longer: 6.9 seconds and 181 mm. Figure 2.1 shows the phantom in position on the CT scan machine. For two trials, radiation exposures measured were 1.09 R and 1.08 R in the center hole, and 1.96 R and 1.96 R in the peripheral hole.

Then the OSL dosimeter replaced the ion chamber and the procedure was replicated. The center integrated dose was 1046 mGy (104.6 rad) making the $CTDI_{100}$ 43.6 mGy (4.36 rad). For the peripheral location, the integrated dose was 1686 mGy (168.6 rad) making the $CTDI_{100}$ 70.3 mGy (7.03 rad). Figures B.2 and B.3 contain the results as reported by Landauer.

Figure 2.1: The FDA phantom in the CT gantry waiting for imaging.

Chapter 3

Verification Stage

In the verification stage of this project, the main goal is to ensure that the deterministic computation is functioning properly. The code and multigroup cross section library should be capable of simulating correctly the given input model. This does not necessarily guarantee that the results match reality (in this case, the experimental results), only that the program solves the equations as it is instructed.

The verification process aims to evaluate the various physical phenomenon, ensuring that the simulation is correct in each case. This requires some knowledge and prioritization of the expected issues likely to cause problems. For this verification, the first step is the creation of a simple model. The model is a right circular cylinder with appropriate boundary conditions. The cylinder is composed of tissue-equivalent material. Detectors are designated as volumes within the cylinder, locating them such that they are comparable to the detectors in the Rando phantom experiment. This preliminary model uses a Monte Carlo method for simulation. This allows the inclusion of the greatest range of physics.

With a basic model constructed, the first test is designed to determine the importance, or as shown, the lack of importance, of secondary electron transport. The Monte Carlo method is extremely useful for this task. Next, a deterministic model is built, and various comparisons are made between the two methods. One major comparison concerns the multigroup energy discretization of the deterministic model. The main challenge here is the preparation of an appropriate multigroup cross section library. In addition, the spatial and angular meshes are examined to achieve necessary resolution and results while limiting execution time.

3.1 Preliminary Monte Carlo Model

The verification stage begins with a Monte Carlo model, since the Monte Carlo method has a number of advantages over deterministic methods. Note that the two methods are complementary—where the deterministic code is weak, Monte Carlo can fill in the gaps. Later, when computational efficiency is the goal, the advantages of the deterministic models will be realized. Using Monte Carlo methods, one can fully utilize the available nuclear data, i.e. continuous energy dependence of the cross sections, without resorting to energy discretization into energy groups. Also significantly, Monte Carlo methods are able to account directly for secondary charged particle transport, a feature which deterministic neutral particle transport codes such as TORT lack without complex manipulations of the cross sections and extensions to the transport equation. These features allow a quantification of the accuracy of the hypothesis that secondary electrons produced by the x-ray source are not sufficiently energetic to result in non-local energy deposition.

In Section 3.1.1, the simplified model used for verification of the above mentioned hypothesis is described, both in the motivation and rationale as well as the geometrical and material specifications. Next, the main question regarding the importance of the secondary electron transport is addressed in Section 3.1.2.

3.1.1 MCNP5 Model

As noted before, MCNP5 is capable of modeling secondary electron transport in a straightforward manner. Therefore, MCNP5 is a valuable tool for examining the validity of the local secondary electron energy deposition assumption in the CT scan of the Rando phantom, and by extension human subjects.

Model Rationale

To test the local energy deposition assumption by secondary electrons, a simplified model was desired which enables easy creation and modification. Modeling the geometric complexities of the phantom is unnecessary for the purposes of this preliminary task. Additionally, for the ultimate goal of conducting comparisons of the computed dose with TORT, the deterministic discrete ordinates code, it is desirable to eliminate as many extraneous factors as possible. Testing simple geometries allows more accurate verification of the com-

putational models. To preserve the general geometrical shape and size of the phantom, a set of concentric right cylinders was employed. The source geometry is assumed to be stationary, monoenergetic, and angularly isotropic. All of these simplifications are imprecise. However, the rotation of the source x-ray tube contributes little to the initial verification tests, so it is ignored. By modeling the highest energy photons only, the source description is simplified while still testing the local energy deposition assumption. If the highest energy photons do not result in non-local secondary electron transport, then the lower energy photons will similarly not result in non-local energy deposition. With limited knowledge of the actual source but using guidance from the literature (see Section 1.3.3), 150 keV was estimated to set an upper limit on the photon source energy. In the CT machine, the photon beam is collimated, but this also plays no role in this verification exercise. These assumptions greatly simplify the input and allow easier comparison to TORT. The detectors are modeled as small cylinders located within the body cylinder. Two internal locations were chosen at different depths from the body-cylinder's outer surface to be representative of the several positions of the actual detectors employed in the experimental measurements on the Rando. This approximate problem setup is illustrated in Figure 3.1.

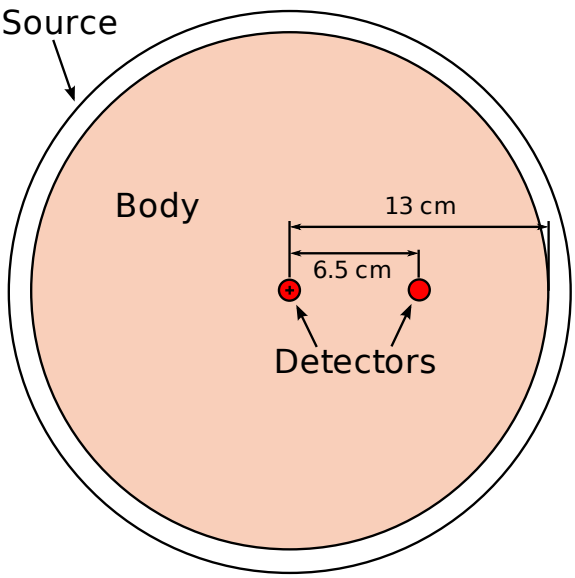

Figure 3.1: The simplified body cylinder MCNP model.

Model Description

The body cylinder has a radius of 13 cm. The Rando phantom slice of interest is approximately a rectangle of width 31 cm and height 22 cm. These two values were averaged to give an average side length of 26.5 cm. The radius of 13 cm then makes the model similar in magnitude to the phantom dimensions.

It is essential to model the same material composition used in constructing the phantom. In MCNP, the elements and their corresponding fraction in the target material's nuclear composition are specified by the user in the input file. The material composition modeled was taken from the technical bulletin of the Rando phantom [40]. The elements and their weight percents are listed in Table 3.1. The overall density is also modeled as 0.997 g/cc, the exact listed density of the phantom [40].

Table 3.1: Model material specifications [40].

Element	Weight Percent
Carbon	67.78
Oxygen	20.31
Hydrogen	9.18
Nitrogen	2.50
Antimony	0.22

To enable representation of the simplified geometry as a two-dimensional problem, with variation in the radial plane only, the cylinder height in the MCNP input is set to 60 cm. This sufficiently limits variation along the axial direction near the middle of the cylinder. Vacuum boundary conditions are specified on the problem domain boundaries. A one inch tall slice located at half the cylinder's height represents the location of each detector. The detectors are modeled as two cylindrical volumes, one concentric with the body cylinder and one located at the midpoint of a radial ray. Each of these detectors is 2.54 cm tall, and has a radius of 0.5 cm. The detector volumes are assigned the same material composition as the rest of the body cylinder. The detectors are significantly larger than the actual detectors used in the experimental measurements [19]. This was done intentionally because small detectors in MCNP5 require many more histories to achieve comparable confidence levels

due to fewer particles entering the detector volume and contributing to the tally. To keep the program execution time reasonable, a compromise on larger detectors was made.

Outside the 13 cm radius cylinder is a void, which closely models air. A concentric cylindrical shell of outer radius 14 cm bounds the problem domain. Any particles which leave this cylinder are immediately terminated.

Many of the details of the actual photon source used in the experimental measurements are unknown [19]. For the simplified model, the photons are assumed to be monoenergetic. The higher energy range of the spectrum employed in the current study will thus create more energetic secondary electrons that are more likely to travel farther from their point of birth, thereby testing the conjecture more stringently. With the limited knowledge of the CT scan source detailed energy spectrum, 150 keV was estimated to be the upper limit and so would serve well as the source energy.

The source was defined as a cylindrical shell concentric with the body cylinder with an outer radius of 14 cm and an inner radius of 13.99 cm, thus effectively creating a cylindrical shell source, which is not natively available in MCNP5. The source cell is a void, so no particle attenuation occurs as photons travel from the source shell to the body cylinder. The limitation of this cell method is that the particles are emitted isotropically because no predefined vector exists to aim the particles inwards. In contrast, for MCNP5 surface sources, a vector is defined normal to the surface as a reference direction by which one can specify source angular emission distributions.

As a result of using this simpler method, less than half the particles emitted from the cylindrical shell actually enter the body cylinder. However, the actual penalty for this is rather low because the wayward particles are terminated immediately after exiting the 14 cm cylinder. The actual number of particles entering the body cylinder is just less than 40% of the particle histories specified in the input to MCNP.

3.1.2 Determining Importance of Secondary Electron Transport

The main goal of this stage in the study using MCNP5 is determining the effect of secondary electron transport on the computed absorbed dose. For photons and electrons, MCNP has two different energy tallies. The tallies track different quantities characterizing a sampled particle, but both return the amount of energy deposited in a cell volume. One can exploit the differences in the tallies, as well as the photon-only versus photon-electron modes,

to determine the significance of secondary electron transport. The proceeding sections detail both of these approaches.

Two Energy Tallies

Two distinct MCNP5 tallies are available to measure energy deposition. First, the F6 tally records energy lost during individual interactions of the sampled particle with the cell's material content. The tally is based on the total track-length of the particles while they travel through the cell's volume [24]. The track length gives an estimate of the scalar flux, which relates directly to particle interaction rates and deposited energy. This tally gives the solution to the integral:

$$H_t = \frac{1}{m} \int dE \int dt \int dV \int d\hat{\mathbf{\Omega}}\, \sigma(E)\, H(E)\, \psi(\vec{r}, \hat{\mathbf{\Omega}}, E, t), \tag{3.1}$$

where m is the cell mass, $\sigma(E)$ is the total macroscopic cross section, $H(E)$ is the heating number (the average energy transferred per collision), ψ is the angular flux, $\vec{r}$ is the spatial position, V is the cell volume, $\hat{\mathbf{\Omega}}$ is the unit vector pointing along the direction of particle motion, E is particle energy, t is time, and H_t is the total energy transfer from the incident particles to the cell volume per unit mass. The use of the heating number $H(E)$ in the integration shows that this is the kerma, not the absorbed dose. Of course, MCNP does not calculate this integral directly. The F6 tally records the amount of energy lost during photon interactions which occur in the detector cell. According to page 2-86 of Volume 1 of the MCNP5 manual [24], all energy transferred to electrons is assumed to be deposited locally. Thus, the F6 tally is a measure of the kerma.

In contrast, the *F8 tally maintains a net sum of the energy of the particles entering and leaving a volume. An entering particle's energy is added to the total, while an exiting particle's energy is subtracted. This tally tracks the original particle as well as its progeny of secondary particles. Therefore, this tally does not assume secondary electron energy deposition to be local. This is useful because it enables two separate methods to test the validity of the hypothesis. First, using the photon-electron mode in which MCNP tracks the trajectories of both particle types, the *F8 and F6 tallies can be compared. If the kerma of F6 is equal to the energy deposition of *F8, then charged particle equilibrium (CPE) for electrons exists. Second, the *F8 tally can be used to compare the dose computed via the photon-only to the dose computed via the photon-electron mode. In the photon-only

mode, all energy transferred to electrons generated as secondary particles is assumed to be deposited locally implying short electron trajectories from point of birth to point of total absorption. This approach also allows finer verification using the energy binning within the *F8 tally produced by MCNP. The events tallied by *F8 are placed in bins according to the energy of the event. The distributions given by these bins give more detail of the dose energy distribution than the total absorbed dose alone.

F6 to *F8 Tally Comparison

The MCNP5 manual states that the F6 and *F8 tallies should give the same total deposited energy provided CPE exists. Using the photon-electron mode, the *F8 tally does take into account secondary electron transport, while the F6 tally is simply a measure of the kerma. The present case was executed in photon-electron mode, and the F6 and *F8 tallies were compared for each of the center and radius detector volumes. These two tallies are produced in different units (energy per unit mass for F6 and simply energy for *F8). For comparison purposes, the *F8 tally is calculated on a per unit mass basis by dividing by the cell mass, which is equal to the density of the body cylinder material (0.997 g/cm^3) times the volume of the detector. The simulations were executed with 10^{10} particle histories.

For the center detector, the relative difference between the F6 and *F8 tallies is 1.2%, and for the radius detector it is 0.8%. These errors are greater than the statistical uncertainty estimated by MCNP as 0.05% for the center detector and 0.18% for the radius detector. However, the relative difference of only a percent, while statistically significant, is practically negligible. The other components of the model have error much larger than one percent, so neglecting this difference should have minimal impact on the final results. Table 3.2 provides the tally data comparison for the photon-electron mode case. This close agreement is evidence that CPE exists and that secondary electron transport can indeed be neglected.

Photon-only to Photon-Electron Mode Comparison

The second method of confirming that secondary electron transport is negligible in computing the deposited energy from a CT scan is utilizing the MCNP5 execution options of photon transport only and photon-electron transport. In the photon-only mode, energy

transferred to electrons is assumed to be deposited locally. The *F8 tally is used to compare these two modes, as it tallies all particles entering and leaving the detector volume. Because the F6 tally does not track secondary electrons, it is not useful in this comparison.

Again, the simulations were executed with 10^{10} particle histories. The relative difference between the computed dose using these two modes for the center detector is 0.3%, while the MCNP statistical uncertainty for that detector is 0.18%. For the radius detector, the relative difference is 0.1%, and the statistical error is 0.17%. This statistical agreement again confirms the assumption. It is clear that the total energy deposited is practically the same for both modes. Avoiding the electron transport yields no significant difference in the computed total energy deposition. The results of these numerical experiments are summarized in Table 3.3.

In addition to the total energy deposition, MCNP also tracks the energy distribution for the tallies, keeping record of interactions in distinct, user-specified energy bins. For the *F8 tally, each energy deposition, which is calculated for one event as the energy difference between the incoming particle energy and the sum of all the outgoing progeny particle

Table 3.2: The F6 and *F8 tally comparison confirms that CPE exists.

	F6		*F8		
	Dep. Energy (eV/g)	Relative Error	Dep. Energy (eV/g)	Relative Error	Relative Difference
Center	0.5785	0.0005	0.5855	0.0018	0.012
Radius	0.6487	0.0005	0.6539	0.0017	0.008

Table 3.3: The photon-only to photon-electron mode comparison using the *F8 tally also confirms the insignificance of accounting for secondary electron transport.

	Photon-only		Photon-Electron		
	Dep. Energy (eV/g)	Relative Error	Dep. Energy (eV/g)	Relative Error	Relative Difference
Center	0.5837	0.0018	0.5855	0.0018	0.003
Radius	0.6533	0.0017	0.6539	0.0017	0.001

energies, is placed in the incident particle's corresponding energy bin. This distribution does not offer much physical insight, but it gives finer detail to the examination of the differences between the two modes. Figures 3.2 and 3.3 show the energy deposition distribution for the photon-only versus photon-electron mode in the center and radius detectors, respectively. The plots with the included one standard deviation error bars clearly show that the distributions do not change from photon-only to photon-electron mode. Because the energy dependence of the response functions of the experimental TLD's are unknown, it is reassuring to observe a similarity of the dose distributions over the relevant energy range. The comparisons depicted in Figures 3.2 and 3.3 show that whatever the energy dependence of the response function is, the absorbed dose will be computed approximately the same with or without secondary electron transport. While the total energy deposited agreement provides sufficient evidence of CPE, the detailed agreement evident in Figures 3.2 and 3.3 offers elevated confidence that the calculations can be accurately performed without the inclusion of secondary electron transport.

Energy Deposition Distributions

While the *F8 tally energy binning gives limited insight into the details of the interactions, the F6 tally binning represents a more physically insightful quantity. Each interaction is placed into a bin based on the energy of the incoming photon. Figure 3.4 shows the energy deposition in the center detector for both photon-only and photon-electron modes (which should be identical based on the definition of the F6 tally), and Figure 3.5 illustrates similar data for the radius detector. It is clear from the plots that the largest amount of energy is deposited by uncollided photons. Below the uncollided energy of 150 keV, the distribution is essentially flat until approximately 60 keV, when the energy deposition drops appreciably. These results are more useful for comparison to TORT and experimental values than the energy distributions of the *F8 tally. With the TORT-computed scalar flux $\phi(E)$ in the detector region, this same energy distribution could be obtained by multiplying the flux by the energy dependent macroscopic interaction cross section and response function.

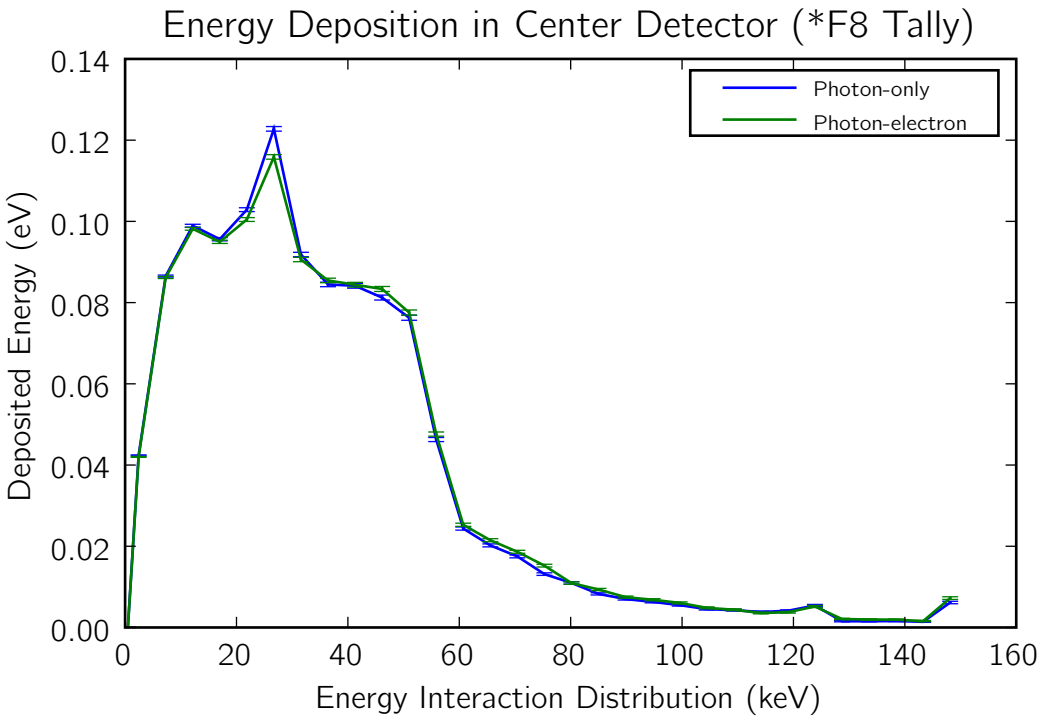

Figure 3.2: A comparison of the photon-only versus photon-electron energy deposition in the center detector as measured by the *F8 tally. The energy of each event captured in the *F8 tally distribution is the energy difference of the incident and all emitted (if any) particles.

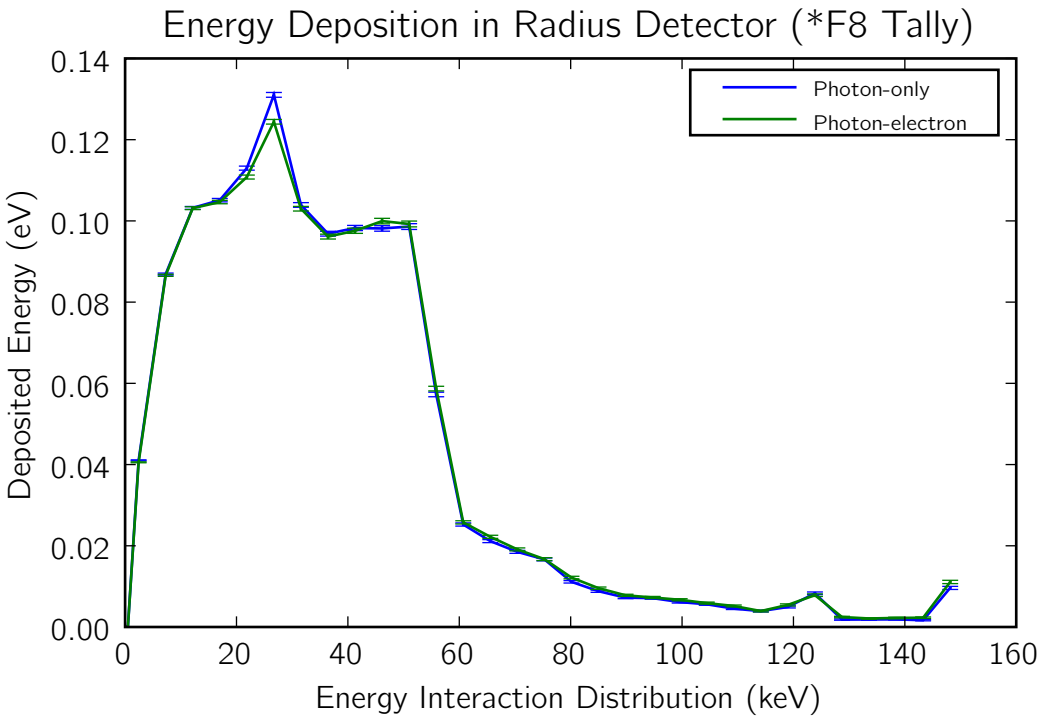

Figure 3.3: A comparison of the photon-only versus photon-electron energy deposition in the radius detector as measured by the *F8 tally.

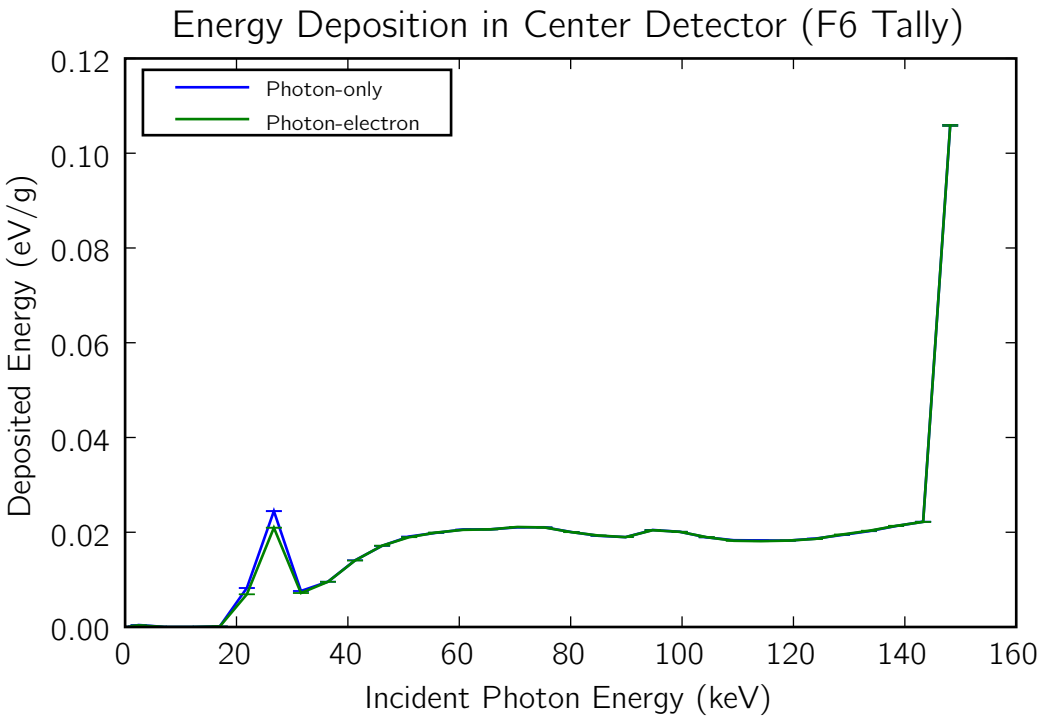

Figure 3.4: A comparison of the energy deposited in the center detector as a function of the incident photon energy for the photon-electron and photon-only cases.

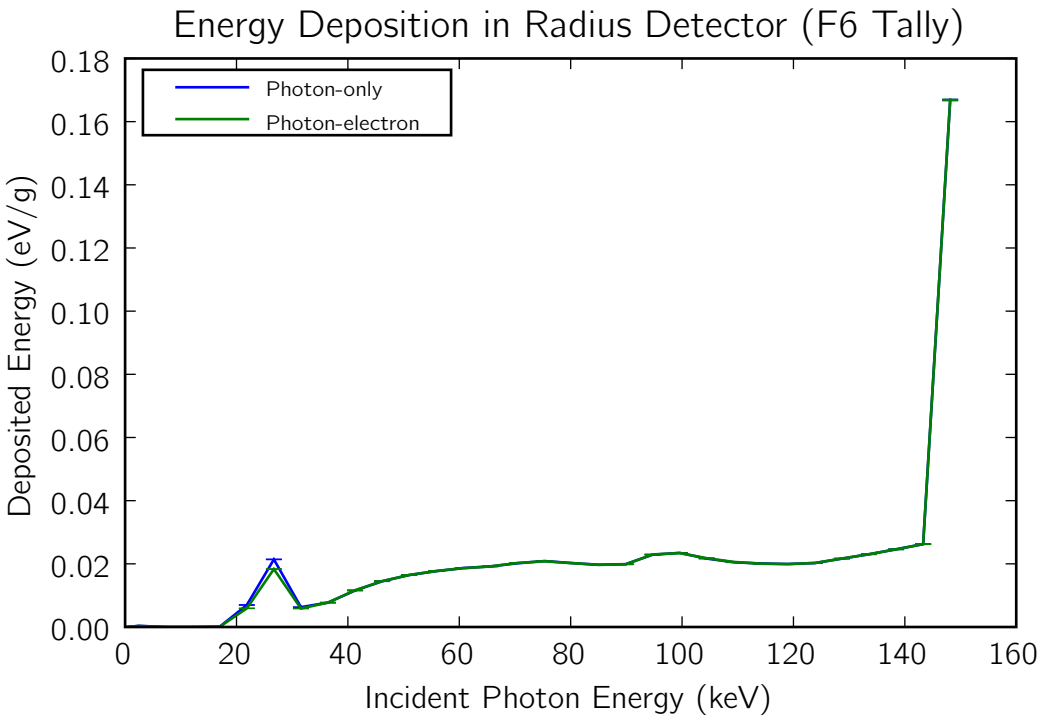

Figure 3.5: A comparison of the energy deposited in the radius detector as a function of the incident photon energy for the photon-electron and photon-only cases.

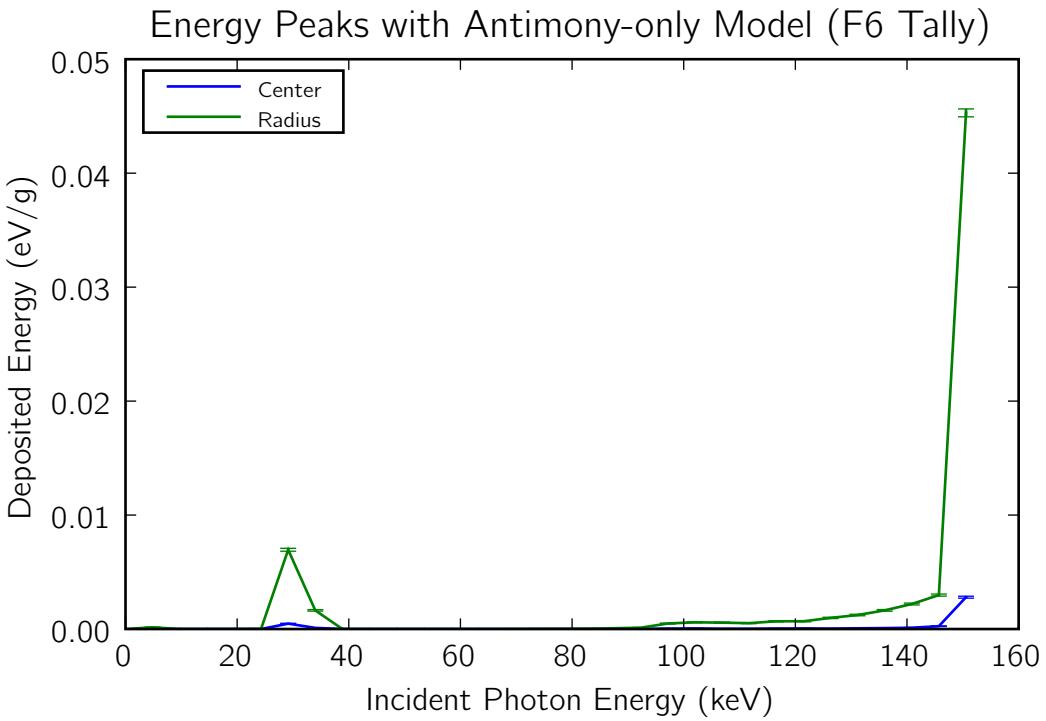

Figure 3.6: The F6 energy deposition spectrum for the antimony-only model. Note the peak at 30 keV.

Antimony Peak at 30 keV

When examining the energy spectra of the F6 tally (Figures 3.4 and 3.5), a noticeable exception to the smooth distribution is the peak at the 30 keV bin. The isolated nature of this peak makes it likely that it is caused by a particular excitation energy of one of the elements comprising the phantom's material. To determine which element is responsible for this peak, the model was run with only one of the elements at a time, testing all five elements contained in the material. Only the antimony case produced the same characteristic peak at 30 keV. Figure 3.6 shows the peak in the F6 tally using the photon-only mode with only the antimony in the body cylinder. Further investigation confirms that antimony indeed has characteristic x-rays at 26 and 30 keV [41].

Internal Voids

Although not directly applicable to the analysis of the Rando phantom, the effects of internal voids were also examined. This could be significant when considering absorbed dose near internal body cavities, which could be a potential extension of this work. Cavities are significant because sharp material interfaces signify potential loss of CPE that might imply the necessity of accounting for secondary electron transport in computing energy deposition. To determine the effects of an internal void on the validity of the assumption that electron transport is negligible in computing deposited energy, a cylindrical cell was inserted between the center and radius detectors into the model illustrated in Figure 3.1. The new cell material properties were specified as vacuum. A number of different variations were tested with differently sized detectors, void cell, and separation between the detectors and void. All the variations showed no deviations from the secondary electron local energy deposition assumption. The most convincing argument can be made by the case with the smallest detector positioned closest to the void. The detectors in this case should be the most sensitive to gradients at the interface when compared to the other configurations. In this most sensitive case, the detector diameter was 0.5 cm, and both detectors were touching the void cell. This geometrical setup is illustrated in Figure 3.7*a*. To test the local electron deposition assumption for this case, a similar argument is constructed as for the standard case discussed previously. First, the F6 and *F8 tallies are compared, and then the photon-only to photon-electron modes are compared using the *F8 tally.

Voids: F6 to *F8 Tally Comparison

The kerma calculated by F6 is compared to the total energy deposition computed by the *F8 tally in the same ways as in Section 3.1.2. The explanation of the comparison will not be repeated here. For the center detector, the relative difference between the F6 and *F8 tallies is 0.7%, and 0.8% for the radius detector. These errors are of comparable magnitude to the statistical uncertainty given by MCNP as 0.2% for the center detector and 0.2% for the radius detector. This is a statistically significant difference, being more than four standard deviations apart. However, even with this slight difference, the error is still less than one percent. Table 3.4 provides the data comparison for the photon-electron mode case. This close agreement is evidence that CPE exists even in the vicinity of the void

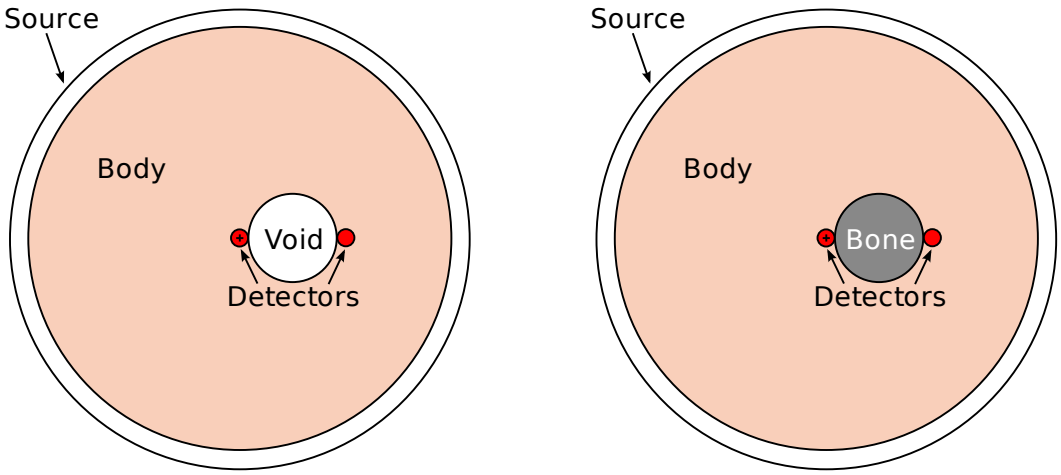

(a) Cylindrical phantom with void.

(b) Cylindrical phantom with bone.

Figure 3.7: The simplified body cylinder MCNP model with an internal void and bone.

and that secondary electron transport can be neglected in computing energy deposition.

Table 3.4: The F6 and *F8 tally comparison confirms that secondary electron transport can be ignored for the determination of absorbed dose near internal cavities.

	F6		*F8		
	Deposited Energy (eV/g)	Relative Error	Deposited Energy (eV/g)	Relative Error	Relative Difference
Center	0.6159	0.0005	0.6204	0.0017	0.0074
Radius	0.6643	0.0005	0.6695	0.0017	0.0078

Voids: Photon-only to Photon-Electron Mode Comparison

For the complete argument concerning the photon-only to photon-electron mode comparison, see Section 3.1.2. The relative difference between the different modes for the center detector is 0.03%, while the MCNP statistical uncertainty for that detector is 0.2%. For the radius detector, the relative difference is 0.04%, and the statistical error is 0.2%. This statistical agreement again confirms the tested assumption. It is clear that the total

energy deposited is the same for both modes. The results of these tests are summarized in Table 3.5.

Table 3.5: The photon-only to photon-electron mode comparison using the *F8 tally also confirms the unimportance of tracking secondary electron transport even in the presence of internal voids.

Mode:	Photon-only		Photon-Electron		
	Deposited Energy (eV/g)	Relative Error	Deposited Energy (eV/g)	Relative Error	Relative Difference
Center	0.6202	0.0017	0.6204	0.0017	0.0003
Radius	0.6698	0.0017	0.6695	0.0017	0.0004

Figures 3.8 and 3.9 show the energy spectrum of the incident photons generating secondary electrons for the center and radius detector, respectively. The differences between the photon-only and photon-electron cases are again negligible. Smaller detector volumes were also employed to attempt to detect effects closer to the void surface, but the results showed no significant change. Based on these results, one can conclude that internal voids do not present an obstacle to the use of the local energy deposition assumption for secondary electrons.

Bone

Another possible cause of perturbations in CPE is the bone structure of the patient. A bone causes material discontinuity, so CPE may not be valid in the area around the bone-flesh interface. In a similar manner as the void tests, a volume with bone-like tissue is inserted in the model between the two detectors, seen in Figure 3.7*b*. The bone cell composition is taken from a sample problem in the MCNP5 distribution, and is described in Table 3.6.

Bone: F6 to *F8 Tally Comparison

The kerma calculated by F6 is compared to the total energy deposition computed by the *F8 tally in the same ways as in Section 3.1.2. For the center detector, the relative

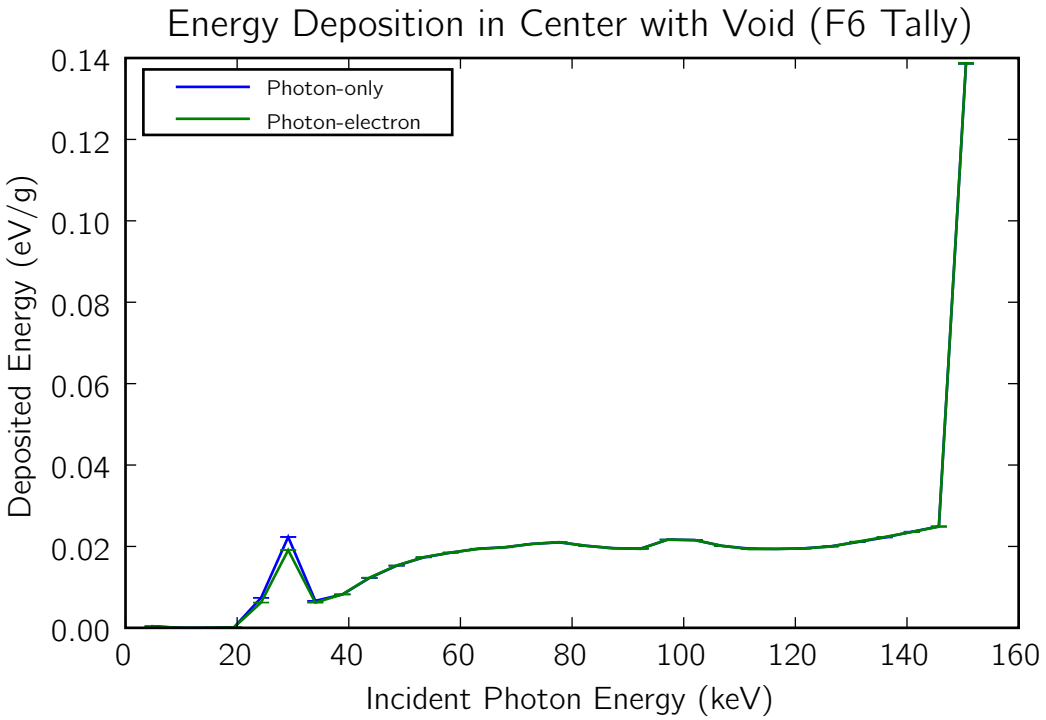

Figure 3.8: A comparison of the energy deposited in the center detector as a function of the incident photon energy for the photon-electron and photon-only cases with an internal void.

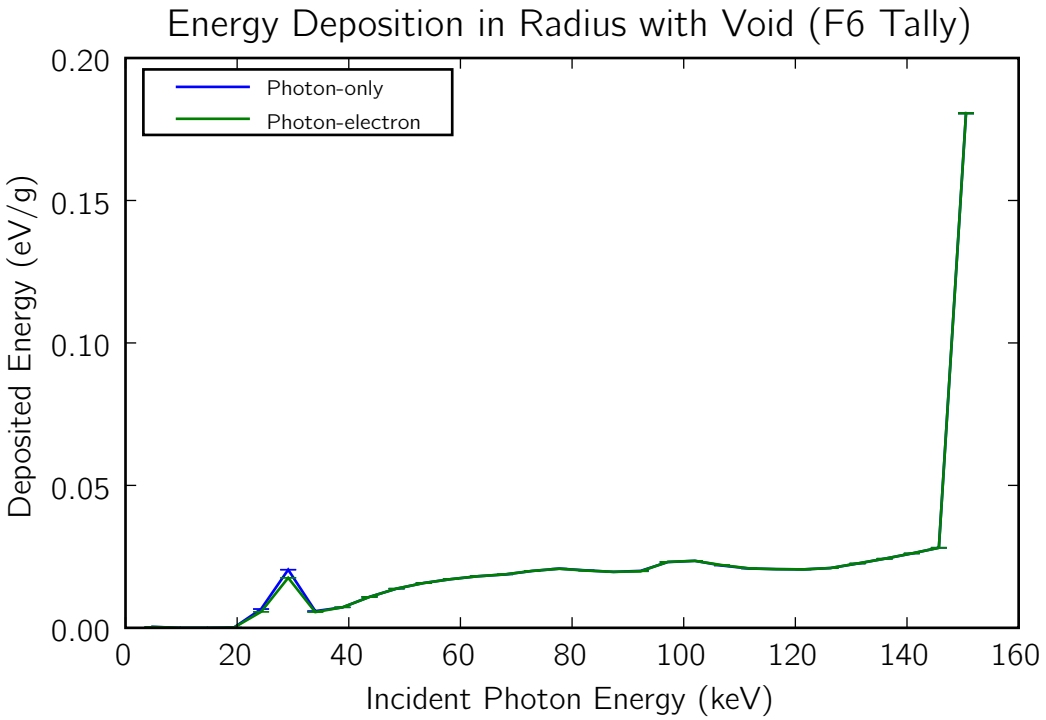

Figure 3.9: A comparison of the energy deposited in the radius detector as a function of the incident photon energy for the photon-electron and photon-only cases with an internal void.

difference between the F6 and *F8 tallies is 1.2%, and it is 0.3% for the radius detector. These errors are of comparable magnitude to the statistical uncertainty given by MCNP as 0.2% for the center detector and 0.2% for the radius detector. There does appear to be a statistical difference between the tallies at the center, but this difference is only one percent. There is no statistically significant difference in the radius detector. Table 3.7 provides the data comparison for the photon-electron mode case. This close agreement is evidence that CPE exists even in the vicinity of the bone and that secondary electron transport can be neglected in computing energy deposition in heterogeneous structures including flesh and bones.

Table 3.6: Bone material specifications.

Element	Weight Percent
Oxygen	59.0
Calcium	22.5
Phosphorus	10.3
Nitrogen	4.2
Hydrogen	3.4
Sulphur	0.3
Magnesium	0.2
Sodium	0.1

Table 3.7: The F6 and *F8 tally comparison confirms that secondary electron transport can be ignored for the determination of absorbed dose near a bone structure.

	F6		*F8		
	Deposited Energy (eV/g)	Relative Error	Deposited Energy (eV/g)	Relative Error	Relative Difference
Center	0.4800	0.0006	0.4859	0.002	0.012
Radius	0.5653	0.0006	0.5669	0.0018	0.0028

Bone: Photon-only to Photon-Electron Mode Comparison

For the complete argument concerning the photon-only to photon-electron mode comparison, see Section 3.1.2. The relative difference between the different modes for the center detector is 0.5%, while the MCNP statistical uncertainty for that detector is 0.2%. For the radius detector, the relative difference is 0.3%, and the statistical error is 0.2%. This statistical agreement again shows that CPE still exists for both detectors. The results of these tests are summarized in Table 3.8. In both cases, the local energy deposition

Table 3.8: The photon-only to photon-electron mode comparison using the *F8 tally also confirms the unimportance of tracking secondary electron transport even in the presence of bone structure.

Mode:	Photon-only		Photon-Electron		
	Deposited Energy (eV/g)	Relative Error	Deposited Energy (eV/g)	Relative Error	Relative Difference
Center	0.4835	0.0019	0.4859	0.002	0.005
Radius	0.5651	0.0018	0.5669	0.0018	0.0032

assumption is still valid. Figures 3.8 and 3.9 show the energy spectrum of the incident photons causing secondary electrons for the center and radius detector, respectively. The differences between the photon-only and photon-electron cases are again negligible. Based on these results, one can conclude that bone structures do not present an obstacle to the use of the local energy deposition assumption for secondary electrons.

3.2 Preliminary Deterministic Model

After confirming that secondary electron transport is unimportant, the next step is to construct a simple deterministic model and compare its results with the Monte Carlo results.

3.2.1 Deterministic Model Description

To aid the comparison with the MCNP simulation, the deterministic model should match it as closely as possible. TORT was selected as the deterministic transport code

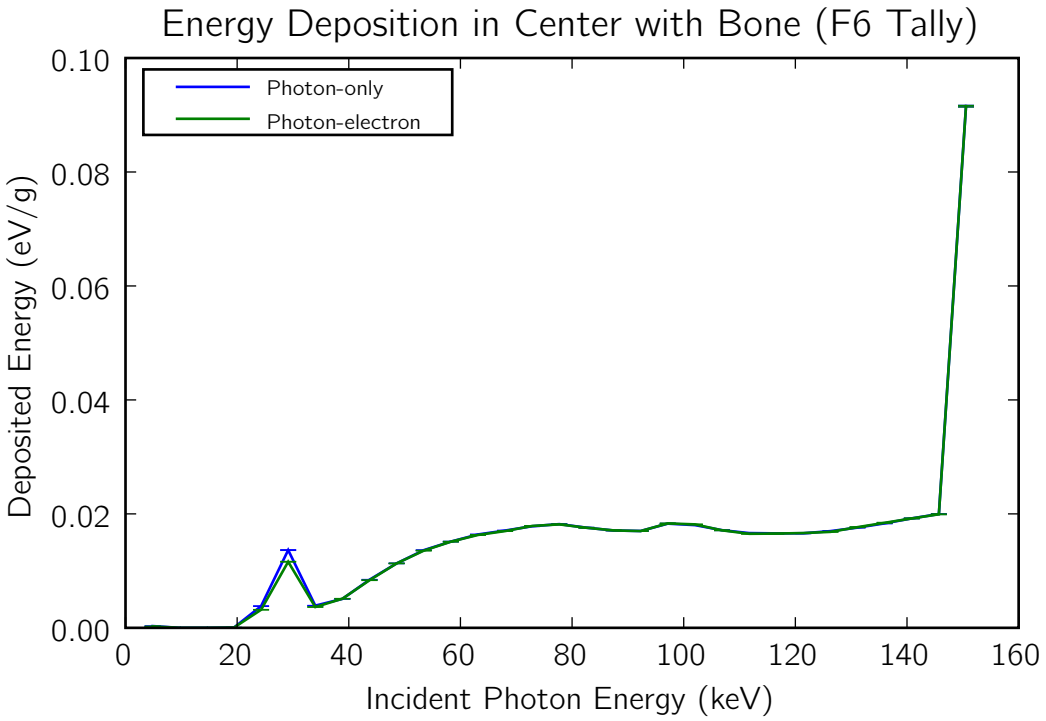

Figure 3.10: A comparison of the energy deposited in the center detector as a function of the incident photon energy for the photon-electron and photon-only cases with an internal bone.

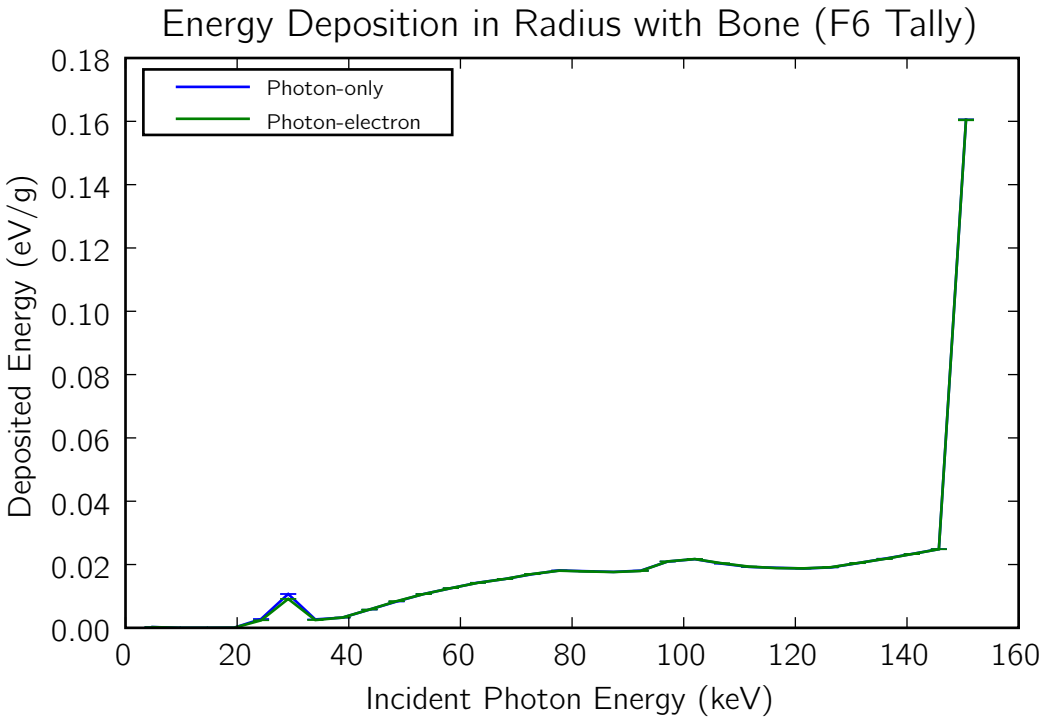

Figure 3.11: A comparison of the energy deposited in the radius detector as a function of the incident photon energy for the photon-electron and photon-only cases with an internal bone.

that executes the model [42]. To build the geometry input for TORT, the companion program BOT3P is helpful [43]. Since TORT only handles Cartesian or cylindrical meshes in three-dimensional geometries, directly creating the input for TORT can be time consuming. BOT3P allows for the description of larger geometric bodies, which it then translates into a set of mesh cells based upon the given mesh spacing. Figure 3.12 shows an example of the three dimensional geometry which BOT3P produces for use by TORT. Note the *staircasing* along the edge of the cylinder, where Cartesian cells must approximate a circular boundary. The x-ray beam is approximated as a distributed volumetric isotropic source contained in

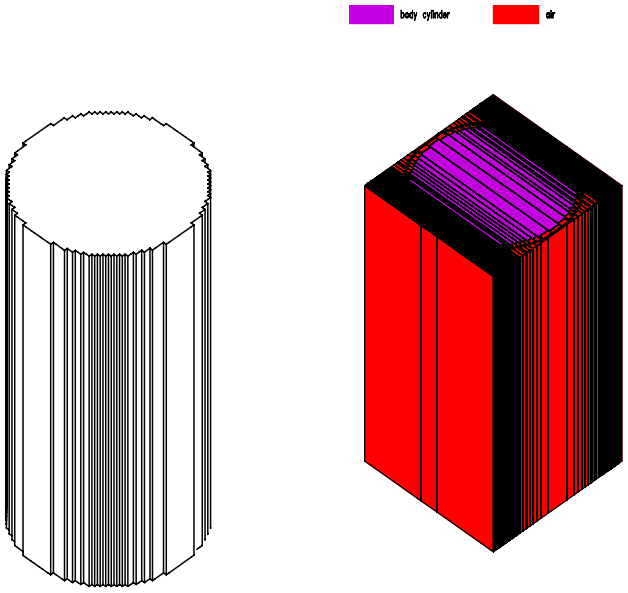

(a) Only the body cylinder.

(b) The body cylinder with the air and source shell.

Figure 3.12: The BOT3P produced geometry.

a cylindrical shell of similar dimensions to the MCNP shell. Again, the photon source is a 150 keV monoenergetic source.

Cross Section Library Preparation

NJOY [44], the nuclear data processing code, was used to convert the point-wise continuous cross sections in the ENDF/B-VII [45] photoatomic data libraries to multigroup

sets appropriate for this application. The two main factors to consider when performing the multigroup collapsing are the energy group structure and the flux energy dependence weighting factor. Many photon cross section sets use logarithmic divisions to encompass a wide range of photon energies. Thankfully, the photon energies of importance in the CT scan only range from about 1 keV to 150 keV. There are no photons above the peak tube potential, for this experiment set at 150 keV. The low energy photons (below 10 or 20 keV) are unimportant for two reasons. First, the photoelectric absorption cross section becomes large at these low energies, which reduces the low energy photon flux to negligible levels. Second, since the goal is to measure deposited energy, these low energy photons have very little energy to deposit. This is the rationale for lumping a large range of low energy photons into one group. With these factors in mind, the group structure is chosen with constant energy width. Ten groups from 10^{-4} eV to 200 keV are selected, with a width of 20 keV for each group. The group structure is provided in Table 3.9. This is the first attempt at a group structure. This could, and probably should, be modified as more details about the prevailing energy spectrum emerge, either merging groups together to increase computational efficiency or splitting groups to gain better resolution. However, the present energy group structure is a reasonable starting point.

Table 3.9: The photon energy group cross section structure in keV.

E_{low}	E_{high}
10^{-7}	20
20	40
40	60
60	80
80	100
100	120
120	140
140	160
160	180
180	200

The other challenge when collapsing multigroup cross sections is to set the weight factors required for the cross section averaging over each group. This is a classic chicken-and-

egg problem, in which the flux energy distribution is needed to compute the cross sections so that the flux energy distribution can be computed. There are two common initial guesses to break out of this dilemma, either a constant flux in energy or a dependence as $1/E$. Based on the Monte Carlo spectrum generated, the constant assumption seemed a better fit, over most of the relevant energy range, for this problem. Thus, the initial cross sections were generated with a constant weight. Later, as the model is refined, the data can be recollapsed using a more realistic photon spectrum. A third order Legendre expansion was employed for representing the anisotropy of the scattering cross sections. An example NJOY input file can be found in Appendix C.

To confirm that this data is reasonable, the total cross section was compared to the continuous total cross section used by MCNP (see Figure 3.13). This gives confidence that the data library was correctly produced.

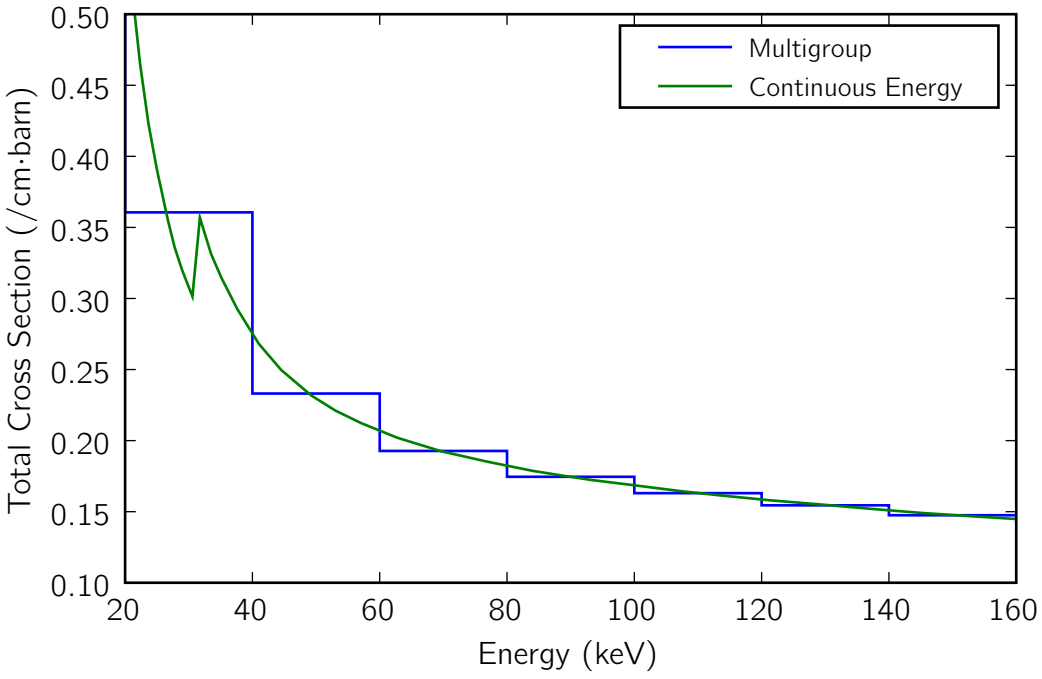

Figure 3.13: The multigroup and continuous total cross sections of the Rando tissue-equivalent material.

3.3 Deterministic-to-Monte Carlo Verification

With the deterministic model constructed, the main step in the verification stage can now proceed. The results of the deterministic and Monte Carlo simulations are compared, and an explanation is sought for any differences observed. One important question is the fidelity of the discretized model in TORT, in angle, space, and energy, as compared to the continuous Monte Carlo model. This error is usually called *truncation error*. Continuous-energy MCNP is used to obtain the reference values against which otherwise computed values are compared to determine the latter's error, while also executing a multigroup MCNP model to examine the multigroup cross section effects. The steps taken in this process are outlined in the following sections.

Multigroup MCNP Using the program CRSRD [46], a multi-group cross section set was prepared which MCNP can read from the ENDF/B-VII data used in TORT. This process is not simply a matter of reformatting numerical data. Since the simulation employed anisotropic multi-group data with Legendre expansion of the scattering cross section, the MCNP format requires that the moments be transformed to probability distributions. There exist a number of methods to perform this transformation which are implemented in CRSRD. Thus, using CRSRD was necessary to produce a multigroup cross section set consistent with that used in TORT to enhance the relevance of the ensuing comparison of computed doses.

With the nuclear data in hand, the computer codes execute the simulations. The simulations fall into two broad categories. First, the deterministic TORT computations that constitute the main thrust of this project were run. Within this category, there is a simulation with a fine spatial mesh and high-order angular quadrature and another with a coarse spatial mesh and lower-order angular quadrature. The coarse mesh had cells of approximately 1 cm on a side, while the fine mesh had 0.2 cm cell sides. The low-order quadrature was the level-symmetric S_6 while the high-order one was level-symmetric S_{16}. The other category is Monte Carlo simulation with MCNP5. This type includes both continuous energy and multi-group cross section data.

Figure 3.14 shows the photon flux in the center of the phantom for all of these simulations, and Figure 3.15 shows the flux for the radius detector. One first notes the "MC

continuous energy many bins" curve, represented by the dotted line, which illustrates the detailed energy spectrum of the flux. This spectral detail is helpful in analyzing the coarse energy grid data.

Examining the deterministic solutions, the coarse and fine mesh results are nearly identical, except for the highest energy group. This is encouraging, as the low resolution model allows for fast computational times while still providing results comparable to a fine mesh solution.

Next, one compares the Monte Carlo continuous results with the TORT results. Above the 20 to 40 keV group, the results are in close agreement. The maximum relative difference in any energy group above 40 keV between the coarse mesh TORT solution and continuous MCNP is 13 percent in the center and 15 percent in the radius detector. For the fine mesh TORT, the maximum error over the same energy range is 11 percent in both the center and radius detectors. In the 20 to 40 keV bin, the TORT fluxes are roughly half that of the Monte Carlo flux. While this is clearly a discrepancy, the low energy and low flux magnitude of this group mean that the total energy deposition will not be significantly altered by this single-group disagreement. The fine-spectrum gives a hint for addressing this minor failure in future research. In this group, there is a rather large spike in the flux spectrum, created by the antimony, causing the constant flux weight assumption used to compute the multigroup cross sections to be inaccurate in this group. If capturing this effect is necessary for validation of the dose, the cross section set can be recollapsed with a better tailored energy spectrum, which will alleviate this problem. As noted below, the spectrum here is not crucial since the x-ray source employed in our model so far is still monoenergetic, a poor approximation of the actual x-ray beam employed in CT scanners.

3.4 CTDI FDA Phantom Verification

All of the simulations to this point have been with a fictional cylinder of the same composition as the Rando phantom. In this section, an actual phantom is modeled. The CTDI FDA body phantom is a right cylindrical homogeneous solid with five drilled holes for the placement of detectors. This is the phantom that was used during the experimental measurements conducted at Hershey Medical Center, and is pictured in Figure 2.1. The CTDI FDA phantom is similar to the model used above, with a few exceptions. The FDA

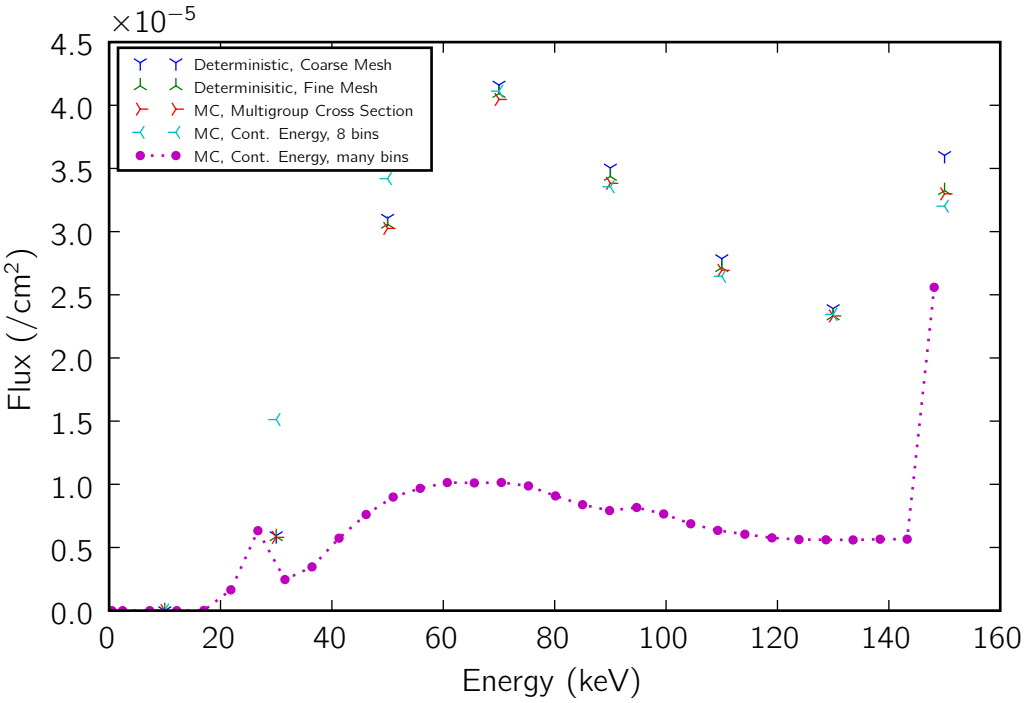

Figure 3.14: The computed flux in the center detector from the various computational tissue-equivalent models.

standards state [39]

> CT dosimetry phantom means the phantom used for determination of the dose delivered by a CT x-ray system. The phantom shall be a right circular cylinder of polymethl-methacrylate of density 1.19+/-0.01 grams per cubic centimeter. The phantom shall be at least 14 centimeters in length and shall have diameters of 32.0 centimeters for testing any CT system designed to image any section of the body (whole body scanners) and 16.0 centimeters for any system designed to image the head (head scanners) or for any whole body scanner operated in the head scanning mode. The phantom shall provide means for the placement of a dosimeter(s) along its axis of rotation and along a line parallel to the axis of rotation 1.0 centimeter from the outer surface and within the phantom. Means for the placement of a dosimeter(s) or alignment device at other locations may

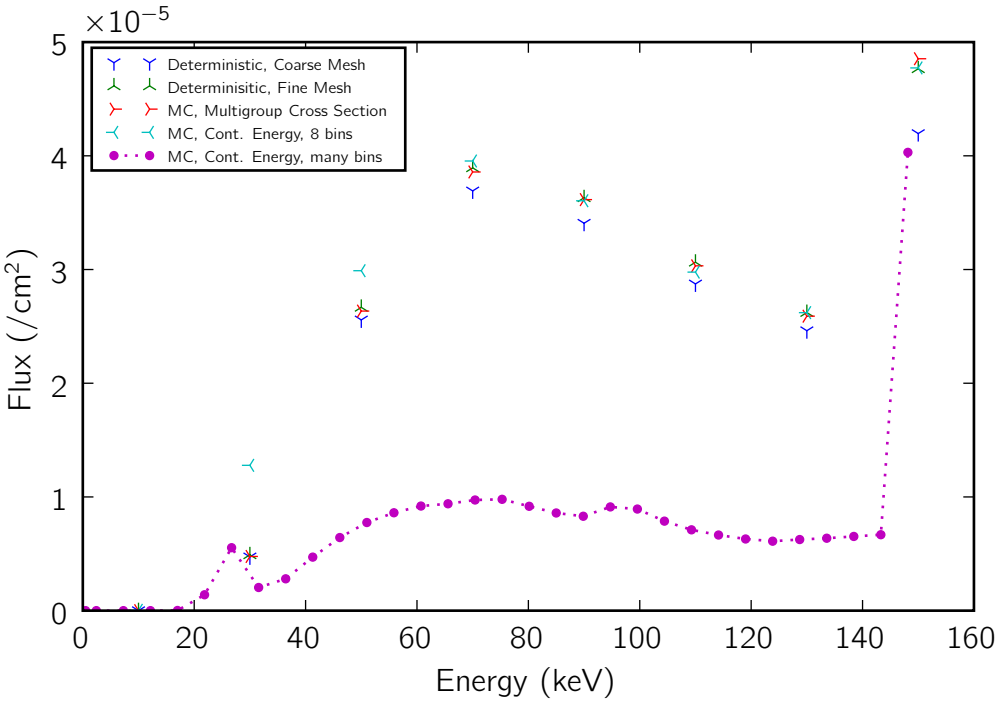

Figure 3.15: The computed flux in the radius detector from the various computational tissue-equivalent models.

> be provided for convenience. The means used for placement of a dosimeter(s) (i.e., hole size) and the type of dosimeter(s) used is at the discretion of the manufacturer. Any effect on the doses measured due to the removal of phantom material to accommodate dosimeters shall be accounted for through appropriate corrections to the reported data or included in the statement of maximum deviation for the values obtained using the phantom.

The chemical formula for polymethl-methacrylate, also known as PMMA and acrylic glass, is $C_5O_2H_8$. Furthermore, the manufacturer's specifications state the height of the particular phantom used in the experimental measurements as 15 cm [38]. The PMMA material has as constituent elements only elements also in the Rando material, so no additional cross sections are needed. They only must be mixed in different ratios. By modifying the previous model, the new FDA simulations are relatively easy to assemble. To instill more realism

in the modeling exercise, a distribution of photon energies characteristic of a tungsten x-ray tube was used. The details of how this distribution was obtained are left for the next chapter, where they fit more closely with the validation exercise.

The results of the Monte Carlo and deterministic simulations are given in Figures 3.16 and 3.17 for the center and edge detector locations, respectively. Plotted in these figures is the group flux computed by TORT on the fine and coarse models described earlier; the group flux computed by MCNP using the corresponding multigroup cross section library; the flux as computed by continuous-energy MCNP simulation then binned over the same multigroup bins, and also over a finer binning. The maximum relative difference (excluding the lowest and highest energy groups) between the coarse mesh deterministic solution and the multigroup MC results is 10 percent at the center and edge detectors. Comparing the fine mesh deterministic fluxes with multigroup MC, the maximum difference (again ignoring the negligible flux in the lowest energy group) is 7 percent at both locations. This good agreement for the flux spectra at both locations between the coarse and fine mesh TORT, and multigroup MCNP results verifies the deterministic and stochastic solution schemes. As for the comparison with continuous-energy MCNP, although all of the higher energy group fluxes computed by TORT exhibit modest agreement with the computed multigroup MC fluxes, the simulated flux in the 20-40 keV group has significant deviations, where the relative error exceeds 100 percent in the center detector location (see Figure 3.16). Unfortunately, this group is important since it accounts for roughly 30 percent of the energy deposition. Thus, it is necessary to compute a multigroup cross section set with weights closer to the actual flux shape.

To collapse this new cross section set, the flux energy weighting factor chosen was the x-ray spectrum leaving the x-ray tube. This spectrum is discussed in Section 4.1. The cross section set was collapsed using NJOY to process the ENDF/B-VII nuclear data. Then the deterministic model of the CTDI FDA phantom was repeated using the new data. The computed flux for the center and peripheral locations are presented in Figures 3.18 and 3.19, respectively. At the periphery, MC continuous-energy flux and the deterministic fluxes match well. In the significant energy range of 20 to 120 keV, the largest relative difference for either mesh is 6 percent. The situation in the center detector is not as favorable. Four out of five of the energy groups from 20 to 120 keV differ by 15 percent or less. However, the 40 to 60 keV group has significantly larger errors, close to 30 percent from the MC

continuous energy reference solution. The x-ray tube spectrum has a large characteristic peak in the 40 to 60 keV range, while the measured flux spectrum at the center detector shows little or no sign of this peak. This is the likely cause of the error in the computed flux in this group. Since this error occurs in the energy group with the highest flux, it will have an impact on the dose estimates. While this new cross section library is used in the validation stage, these results seem to indicate that better deterministic results in the center detector would be possible with a flux weighting which does not include the x-ray tube characteristic peaks. This change would affect the peripheral location as well, but the effects would be less significant than in the center since the photons have a smaller probability of interaction in the thin slice of material separating the edge detector from the outside.

Two further attempts at collapsing a more favorable multigroup cross section set were undertaken. The first was only a slight modification of the previous weighting factor, where the characteristic peaks from the x-ray tube were deleted instead of including them. The computed fluxes in the center of the CTDI FDA phantom with these cross sections are plotted in Figure 3.20. As the figure makes clear, the error in the 40 to 60 keV group is reduced, but it still has a 15 percent error from the reference MCNP solution, down from about 30 percent in the previous case.

The last effort at recollapsing the cross section set employed the MCNP-computed flux at the center of the phantom as the weighting factor. The results for this set are illustrated in Figure 3.21. This eliminated the large errors in the 40 to 60 keV group, reducing the error to a few percent. However, the 20 to 40 keV group then has greater error, about 15 percent. Since this group has less energy and less flux, it would be favorable to have error in this group rather than the 40 to 60 keV when the integrated absorbed dose is the quantity of interest. Certainly these results show that adjusting the weighting factors can improve the accuracy of the results. However, the obvious choices for the weighting factor failed to produce multigroup fluxes with less than 15 percent error.

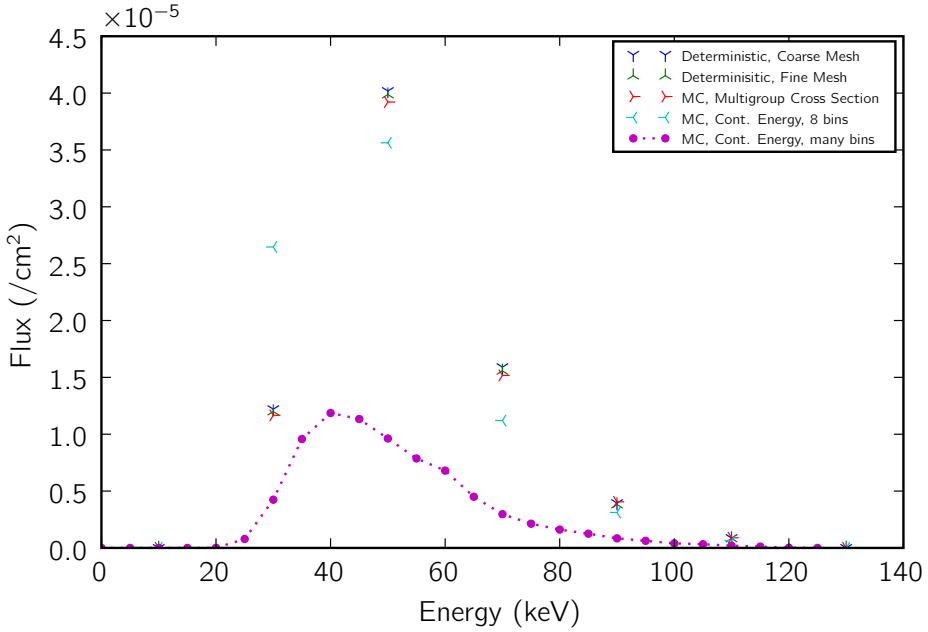

Figure 3.16: The computed flux at the center detector of the CTDI FDA phantom.

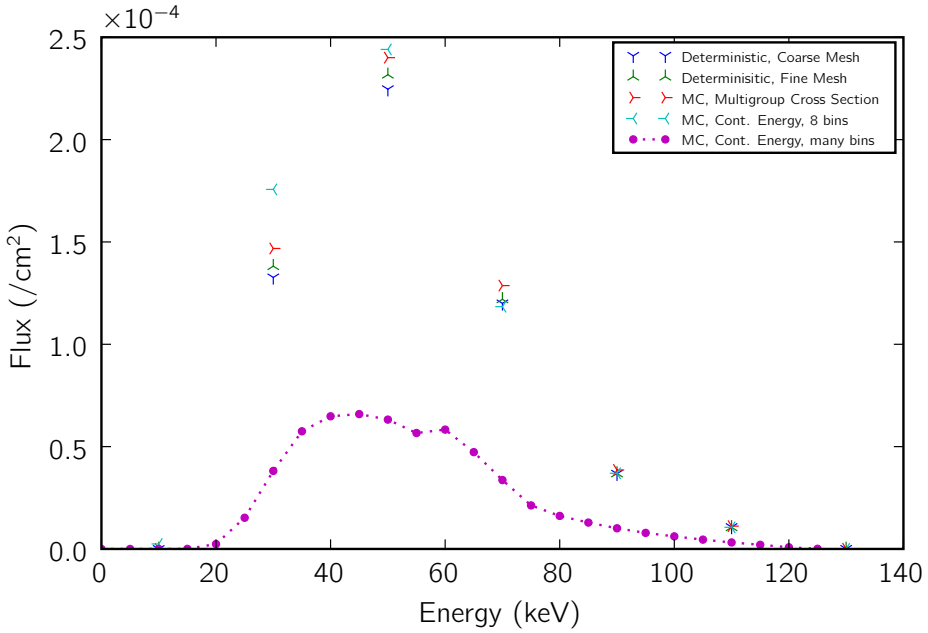

Figure 3.17: The computed flux at the edge detector of the CTDI FDA phantom.

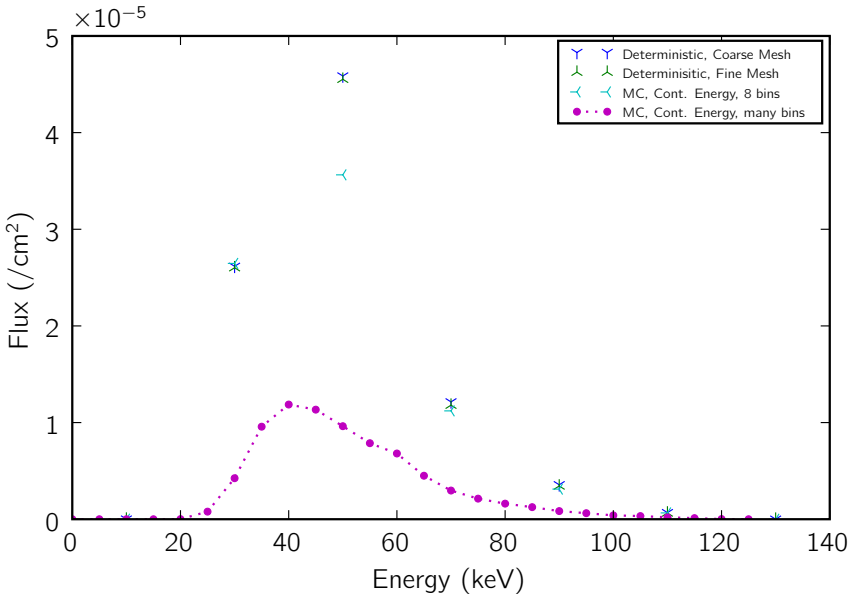

Figure 3.18: The flux at the center detector location of the CTDI FDA phantom as computed with the cross section set weighted by the x-ray tube spectrum.

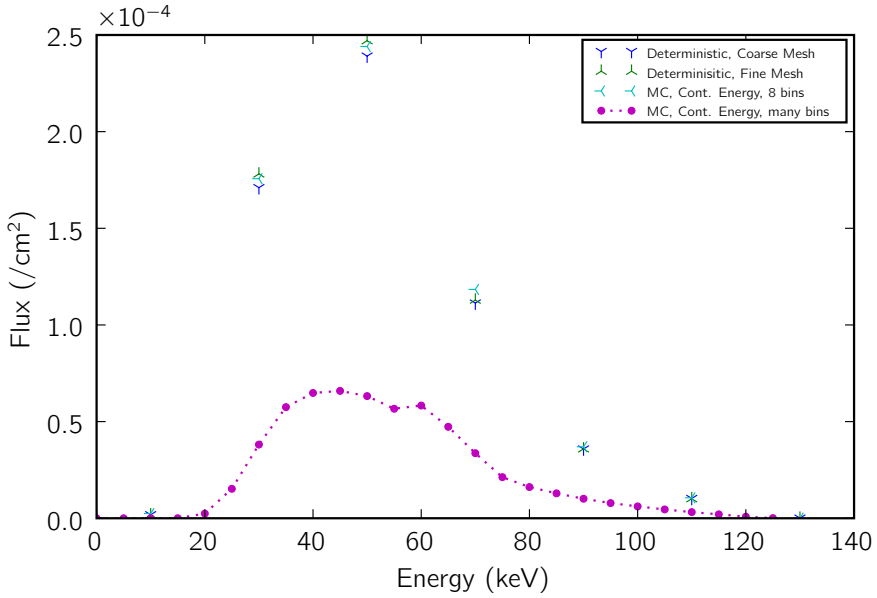

Figure 3.19: The flux at the edge detector of the CTDI FDA phantom as computed with the cross section set weighted by the x-ray tube spectrum.

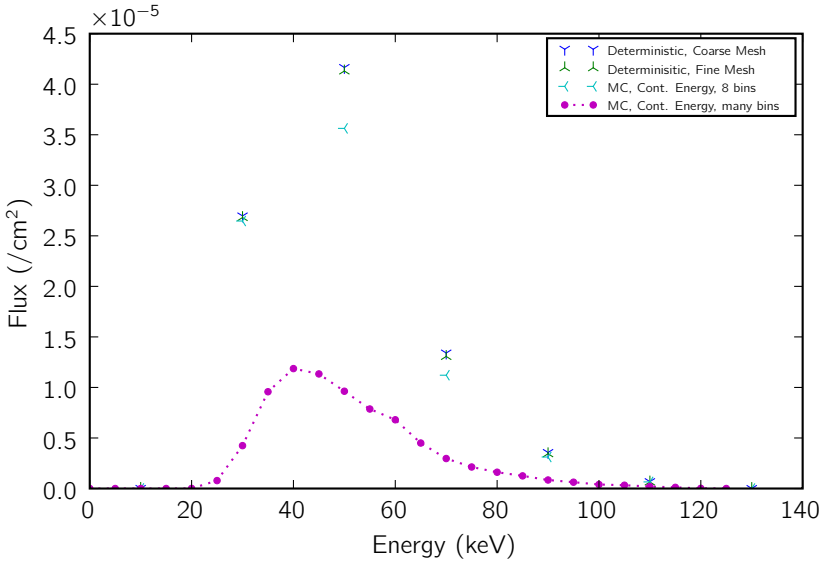

Figure 3.20: The flux at the center detector location of the CTDI FDA phantom as computed with the cross section set weighted by the x-ray tube spectrum without the characteristic x-ray peaks.

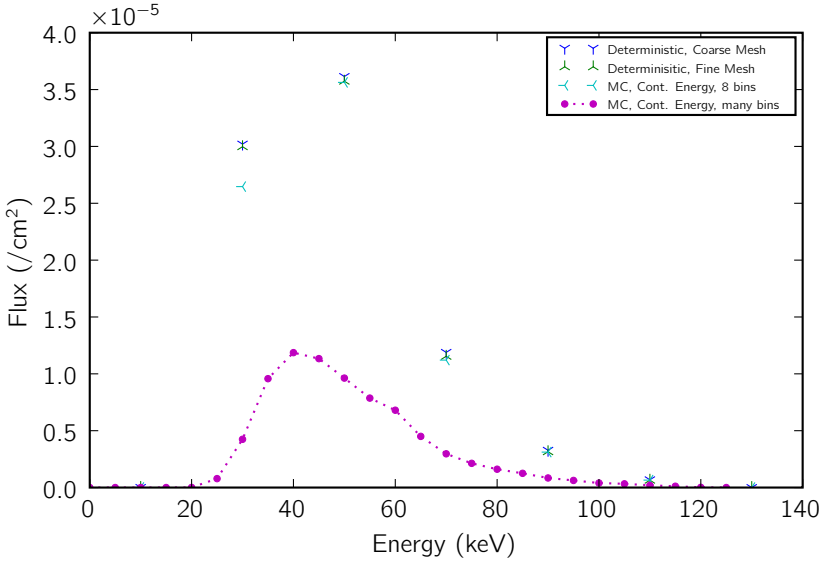

Figure 3.21: The flux at the center detector location of the CTDI FDA phantom as computed with the cross section set weighted by the flux spectrum computed by MCNP in the center of the phantom.

Chapter 4

Validation Stage

Although the CTDI FDA phantom model simulated in the verification stage was realistic in many respects, there are a few areas outstanding which must be addressed before full validation is possible. The phantom geometry and the phantom composition are both well represented. The two most significant aspects to add are the x-ray source spectrum incident on the phantom and the source angular distribution. After examining these issues, the validation exercise is presented.

4.1 X-ray Energy Spectrum

In the early verification exercises, the x-ray beam was approximated by a mono-energetic source with energy greater than the peak energy of the actual x-ray beam. However, since the validation stage requires greater realism, this characterization must be refined to better represent the actual beam spectrum experienced by the phantom during the experiment conducted at the Hershey Medical Center. The most direct and realistic approach would be the measurement of the x-ray spectrum using a radiation detector and multi-channel analyzer during one of the CT scans, positioning the detector at the center of the gantry without any phantom so that the measured spectrum would be similar to the spectrum incident on the phantom. Unfortunately, the radiologists at Hershey lacked the instruments necessary for this direct measurement, so another route must be forged.

The literature is full of methods by which to obtain an x-ray beam spectrum, especially for x-ray tubes with tungsten anodes. Since the machine at Hershey uses a tube

with a tungsten anode, the literature data is applicable to this situation. Given the peak tube voltage, these references provide the photon spectrum leaving the x-ray tube. In a frequently-cited paper on the subject [31], Boone and Seibert present a small computer code written in C that generates the x-ray spectra from a tungsten anode for 30 to 140 kV. This method uses measured x-ray spectra from Fewell *et al.* [47] to interpolate for the desired beam. Using this program, the calculation of the beam spectra is simple. The main program inputs are the peak tube potential in kilovolts and the filtration. The tube potential is a parameter set by the machine operator, so it is known for each measurement. In the experiments at Hershey, the peak tube potential was set to 120 kV. Unfortunately, the second input, the filtration, is a significant factor which varies from machine to machine. The filtration has two components, the internal and external filtration. The internal filtration is that caused by the x-ray tube port [3]. This port is a window from the anode to the outside of the vacuum enclosure that allows the x-rays to escape the tube. It is typically made of glass. The internal filtration is tube-dependent. Not only does the port filtration vary from tube to tube, but it also changes as the tube ages. The external filtration is added by placing material between the x-ray tube and the patient. Often the external filter is aluminum. In the Siemens Somaton scanner, there is an aluminum filter as well as a teflon bowtie filter. Further details about the dimensions of these filters were unavailable.

Since the filter dimensions were unavailable, an indirect method was employed to estimate the total filtration of the CT machine. This method relied on a measurement of the beam HVL, which the radiological staff at Hershey provided. They measured the half-value layer of the incident x-ray beam with multiple aluminum thicknesses, resulting in an HVL of 8.8 mm Al, the thickness of aluminum that reduces the beam intensity by a factor of two. An unfiltered x-ray spectrum has some initial HVL. As the low energy x-rays are preferentially absorbed by filtration, the HVL of the beam increases monotonically. Thus, after the beam passes through the correct amount of filtration, its HVL will have increased such that it equals the 8.8 mm Al measured at Hershey. A simple MCNP simulation performed this evaluation. The test was in a one-dimensional slab with two regions. The first region represented the filtration, while the second region allowed a measure of the HVL. After simulating a range of inherent thicknesses of region one, the equivalent of 5.0 mm Al gives an x-ray beam which has an HVL very close to 8.8 mm Al. Figure 4.1 shows the exposure in the simulation of the 5.0 mm Al-filtered beam. The dotted black line is at

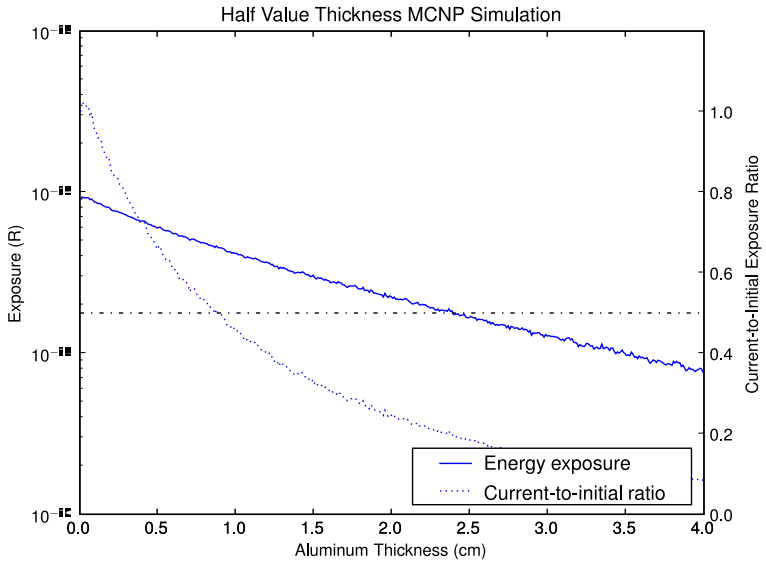

Figure 4.1: The MCNP x-ray beam attenuation simulation with a 5.0 mm thick aluminum inherent filter, looking for a half value layer of 8.8 mm.

a ratio of 0.5, so one can observe that the HVL of this beam is approximately 9 mm Al, sufficiently close to the measured 8.8 mm Al. The filtered and unfiltered spectra are plotted in Figure 4.2. Note how the filtration shifts the spectrum towards higher energies, with the filtered spectrum having a higher average energy.

Source intensity In the verification stage, the simplest manner in which to deal with the x-ray beam intensity was to compute all results on a per-source-particle basis. However, to compare to the experiment, an absolute source strength is needed. Although one could estimate the intensity from the x-ray tube operating parameters (the scan time and current), a more direct route is to use the in-air measurement to scale the source. This requires an extra simulation of the in-air exposure, which is compared to the experimentally measured exposure to obtain an estimate for the absolute source intensity, accounting for the filtration. This simple method, used in the following validation models, is consistent with other researchers' approach [26].

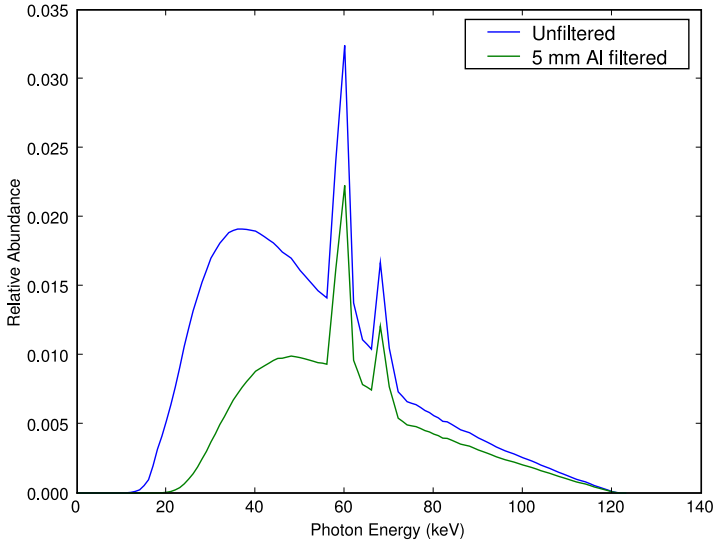

Figure 4.2: The estimated xray source spectra compared with the unfiltered spectra.

4.2 X-ray Beam Direction

The final gap to be plugged in the CTDI FDA model is the angular distribution of the x-ray beam. The beam is collimated in the axial direction, while it fans out in the plane of tube rotation. Since the CT machine is proprietary, only limited details about the beam configuration are available. The rudimentary verification models had isotropic, cylindrical shell sources, mainly because this was the simplest method to have an accurate comparison between TORT and MCNP. However, an isotropic source is no longer sufficient when comparing to an actual experimental device producing a focused beam. Further refinements to the source angular distribution are necessary, mainly the axial collimation into a beam slice. The beam has sharp edges in the axial direction. In addition, since the beam also travels though a bowtie filter, the edges of the fan are reduced in intensity as compared to the fan beam center. A general estimate of the flux intensity from the fan beam center to the edge is available in [48]. The intensity versus position is similar to one-half period of a sine wave, with the flux at the edges about 10% of the intensity at the center. There are many ways to represent these elements in the computational models. Due to the different natures of the computations in MCNP and TORT, the addition of these

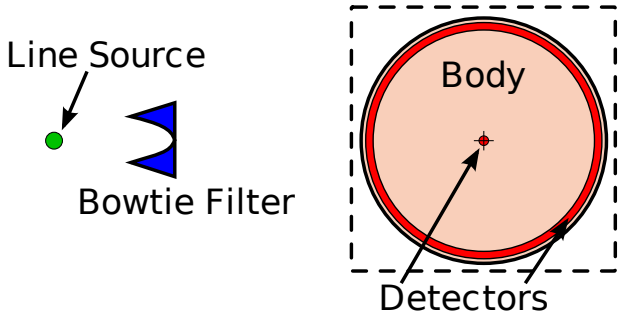

Figure 4.3: A cross section of the MCNP model with collimation and bowtie filter.

beam-shaping elements are implemented in different ways. The following sections outline the approach taken in this work.

4.2.1 MCNP Collimation

Although preliminary simulations ignored the axial collimation and bowtie filter, the poor results quickly suggested that these are important pieces of the model. MCNP offers much flexibility, so there are surely many ways to specify an appropriate source and corresponding phantom. The simplest model captures the relative motion of the source with respect to the phantom, where the x-ray source is fixed (rather than than the spiral trajectory it takes in the machine) and the body phantom is rotated. Since the CTDI FDA phantom is cylindrical and homogeneous, its rotation makes no difference except for the edge detector. To mimick the effect of the edge detector rotation, this small cylindrical detector is replaced with a cylindrical-shell detector, the volume of which is traced by the rotation of the original detector. A cross section of this is pictured in Figure 4.3. To capture the translational motion of the source along the phantom axis, the x-ray beam is represented as a fixed line source parallel to the axis of the cylinder. The length of the line is equal to the CT scan length, 15 cm. The line is 56 cm from the axis of the phantom, a distance representative of the tube-to-center axis distance of a typical CT machine. Since the source is fixed, it is easy to insert a bowtie filter between the source and phantom. The axial collimation is accomplished by permitting source particles to begin only with angular cosines within the range defining the slice width.

However, before reducing the source to a point and adding the bowtie filter, a configuration without the bowtie and with a shell source is simulated first. This model is simpler, allowing a clearer understanding of the effects of the extra components in the more complex model.

4.2.2 TORT Source Angle Biasing

In TORT, without including a collimator, the most obvious method to represent the beam effects is to specify certain directions from the discrete ordinates quadrature set along which the source particles begin. In the TORT input, this is specified by provided direction weights for a boundary source. For the boundary source, the directions which lie closest to the scan plane have weights of one, and other directions have zero weights. This approach presents a number of difficulties. First, no directions in the quadrature set lie precisely in the scan plane. This is necessary to avoid division by zero in the discretized equation set. Unfortunately, the source particles should be traveling in the plane, so this is an obvious discrepancy with reality. The second problem is also a product of the discrete ordinates method. Since only a small fraction of the directions lie close to the scan plane, the majority of the directions are wasted. While it is necessary to have some directions out of the scan plane to capture the effects of scatter, the primary transport of photons is in the scan plane, so it would be desirable to not have the majority of directions pointing away from the plane.

The third problem is a consequence of the first two issues and was discovered early in the TORT validation process. In initial testing for this problem in TORT, it quickly became obvious that ray effects were adversely affecting the accuracy of the results. Ray effects are a byproduct of the discrete ordinates method for angular discretization, wherein particles tend to travel only along the chosen directions in the discrete ordinates quadrature set. This can be a problem in materials that have a low within-group scattering ratio, which is true of the problem at hand. In addition, the detectors are small, so this makes the ray effects more damaging to accuracy because the rays are likely to miss the small detectors.

To ameliorate the issues with the discrete ordinates method, the program GR-TUNCL3D can calculate the uncollided flux and first collision source with ray tracing. This is a semi-analytic method where the flux of photons that have avoided all interactions is computed at each spatial cell using the total cross sections and the exponential radiation

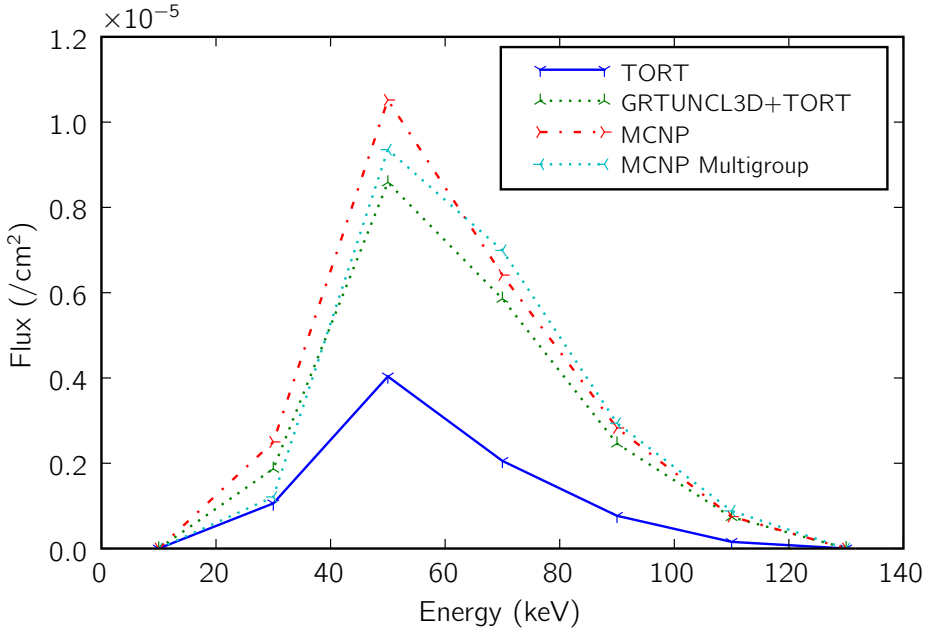

Figure 4.4: The computed flux in the center detector of the FDA phantom. Using the MCNP fluxes as reference, note the improvement in the solution obtained by ray tracing GRTUNCL3D followed by a TORT calculation as compared to results obtained using only TORT's discrete ordinates method.

attenuation law. GRTUNCL3D writes an output file of a distributed source that TORT can read. Then TORT solves the scattering portion of the problem. In the end, the scattered and uncollided fluxes are summed for the total flux distribution. With this additional step, the fluxes computed by TORT and MCNP are in good agreement, where the decrease in flux caused by the ray effects is no longer noticeable (see Figure 4.4). GRTUNCL3D only allows sources to be specified as point sources. However, it does allow angular biasing of these sources. When using GRTUNCL3D, the source is restricted to a narrow range of angles in the axial direction centered around the normal vector to the cylinder surface. This has the same effect as a collimator, but it is more efficient. Since only point sources are allowed, a collection of points along the source circle are included to simulate the rotation of the x-ray tube.

Table 4.1: A comparison of the measured and simulated photon exposures with no collimation.

	Exposure (R)		
Detector	MCNP	TORT	Measured
Edge	5.9	5.6	1.96
Center	0.67	0.69	1.08

4.2.3 CTDI FDA phantom exposure without collimation

First, the initial simulation of the photon exposure is validated against its measured value without beam collimation. The source is normalized to the simulated source such that the in-air exposure, with no shielding or attenuation, is the same as the measured quantity. Then the source in the phantom simulations is similarly scaled. Table 4.1 compares the simulated to measured exposures. While the exposure at the center has an error of about 50%, the calculated result for the edge detector is incorrect by a factor of three. The probable cause of this discrepancy is the unrealistic angular distribution of the beam currently implemented. Since the simulation lacks collimation, it is not surprising that the edge detector experiences a larger fluence than in reality. The next section details the results when the model beam is collimated.

4.2.4 Edge-to-Center Exposure Ratio Validation

In this test, the exposures as measured experimentally are compared with the simulated results using beam collimation. Note that if one works with the ratio of the exposure (or energy deposition) in the edge to exposure (or energy deposition) in the center, then the source normalization is immaterial. For the experimental results, the exposure was 1.96 R at the edge and 1.09 R at the center, giving a ratio of 1.8. Similarly, the OSL strips have a ratio of 1.6. Using the MCNP simulation without a bowtie filter, the fluxes from the seven simulations were added, and folded with the appropriate response function to yield the integrated exposure. For the center, the exposure was 2.17×10^{-16} R and 7.27×10^{-16} R for the edge, both per source photon. The ratio of these two values is 3.3. This is roughly a factor of two from the measured result.

Table 4.2: A comparison of the measured and simulated photon exposures with collimation and the bowtie filter.

	Exposure (R)	
Detector	MCNP	Measured
Edge	1.29	1.96
Center	0.78	1.08

Next, the bowtie filter is included in the computational model as in Figure 4.3. The MCNP-computed fluxes in the center and edge detector locations were folded with the appropriate response function to yield the integrated exposure over the 10-cm long detector. For the center, the exposure was 1.61×10^{-15} R and 2.69×10^{-15} R for the edge, both per source photon. The ratio of these two values is 1.68. In addition, the ratio of energy deposition in the edge to center is 1.73. These ratios are both in very good agreement with the experimentally measured values.

To scale the line source intensity, an in-air exposure simulation was run. The in-air exposure at the center was 8.60×10^{-15} R. Since the in-air measurement was 4.11 R, the source normalization factor is determined to be 4.78×10^{14}. Multiplying the source by this factor yields the results provided in Table 4.2. This model significantly underestimates the exposure at both the periphery and the center. However, errors of 34% for the edge and 28% for the center are not excessive when considering all the model simplifications and imprecise knowledge of several CT machine parameters.

4.2.5 Rando geometry modeling

The anthropomorphic Rando phantom will be more challenging to model than the simple cylindrical phantoms dealt with to this point. To tackle this problem, a rudimentary discretization program has been developed which takes as input a phantom cross sectional image and outputs the spatial stair-cased discretization suitable for the TORT geometric description. The source specification, accounting for the rotation, collimation, and filtration, will be one of the biggest challenges.

Chapter 5

Conclusions

This thesis has detailed a systematic approach to the verification and validation of a CT scan deterministic computational model. A number of experimental measurements were taken at Hershey Medical Center that were used in the validation stage. The verification stage tested a few modeling hypotheses. Finally, the validation stage compared the computed results with the measured exposures and doses.

5.1 Experimental Stage

The experimental stage was a prerequisite to the computational component of this work. A number of measurements were taken using a Siemens Somaton CT scanner, a 16 slice machine. The important measurements were an in-air exposure and dose, with no phantom present, and exposure and dose in the CTDI FDA phantom center and peripheral locations. The in-air measurement was necessary to normalize the source intensity in the computational models. The CTDI FDA phantom was helpful since it is a simple geometric shape, making the model easier to construct than the full detail of the Rando phantom. These measurements were eventually the primary means of validation of the model.

One valuable aspect of the CTDI FDA phantom experiment was the measurement of both the exposure and the dose by different methods. The exposure was measured by an ion chamber while the dose was measured by the OSL strips produced by Landauer. Not only does the measurement of similar quantities by different methods give a better understanding of the uncertainties of the data, but it also aids in the validation exercise,

since there are a number of methods to compute the exposure and dose.

For further work Although the most crucial measurements were obtained, a few additional details would have been beneficial. First, almost no details about the Siemens CT machine were available. This forced the reliance on typical dimensions and beam configurations. Knowing the actual configuration would have been especially helpful for the beam collimators and filters. If these were known, much of the estimates made about the beam would be unnecessary. The second measurement is also related to the beam: a direct measurement of the beam spectrum incident on the phantom. With this information, the largest source of uncertainty in the current model would be reduced. Unfortunately, the high-demand for the CT machine, insufficient instrumentation in the hospital, and the proprietary nature of the CT design conspired against these goals.

5.2 Verification Stage

The verification stage is the most fundamental part of this work. Several key components of the computational model are examined: secondary electron local energy deposition, multigroup energy discretization and cross section library validity, and spatial and angular discretization accuracy. The Monte Carlo method was invaluable in testing these potential issues.

First, a series of computational experiments on a simple tissue-equivalent model examined the validity of the hypothesis of local energy deposition of secondary electrons. The tests were for a location in the center of the cylindrical phantom as well as at the midpoint of a radius. Since MCNP offers the capability to model electron transport directly, but also to disable this option, MCNP is the perfect tool for this job. The same model is executed twice, once with electron transport enabled and once with it disabled. When secondary electron transport is disabled, any energy associated with this electron is deposited at the location where the electron is generated. In a variety of comparisons using both the F6 and *F8 tallies, no significant differences were observed between the photon-only and photon-electron cases, for either the total deposited energy or the deposited energy spectrum. This was sufficient evidence that charged particle equilibrium (CPE) is valid. In addition to a homogeneous cylinder, two other alternate configurations which might be

encountered in CT scans were also examined. These were internal voids and bone, both capable of creating flux gradients and possibly disturbing CPE. However, in the same suite of tests, no significant differences were observed if electron transport was disabled. Charged particle equilibrium is important because modeling a system where CPE is invalid requires accounting for the transport of secondary electrons and is more difficult for deterministic methods. Thankfully, these tests show that the deterministic models can be used without special modifications for secondary electron transport.

Second, the energy discretization of the deterministic problem is examined. Since Monte Carlo avoids energy discretization, MCNP is again valuable for assessing the impact of the energy group discretization approximation. Two models were assembled, one of the tissue-equivalent Rando material and one of the acrylic glass. Both phantoms were cylindrical in shape. Simulations were run in MCNP and TORT. With a constant weighting factor for the multigroup cross sections, the deterministic results were typically less than 15 percent different than the MCNP reference solution. However, in the low energy group from 20 to 40 keV, the error was much larger, greater than 50 percent. Further examination revealed that this error was a result of the incorrect weighting factor used for the cross sections. An initial effort was made to ameliorate this problem by recollapsing the cross sections with the x-ray spectrum of the flux incident on the phantom. While this resolved the problem in the 20 to 40 keV group, it also increased the error in the 40 to 60 keV group. One can note that despite the discrepancy in this one group, the rest of the flux results agreed within 15 percent of the reference solution.

In addition, the effects of spatial and angular discretization were studied. A fine mesh with spatial cells of size 0.25 by 0.25 by 0.6 cm and a S_{16} quadrature set was compared to a coarse mesh with cells 1 by 1 by 1.2 cm and a S_6 quadrature. In almost all the results, the fluxes computed by the different meshes agreed within a few percent. In rare cases, there is a 15 percent difference. Based on this agreement, the coarse mesh would seem to provide sufficient accuracy with obvious performance benefits.

For further work The most obvious and beneficial task is the recollapsing of the cross sections to correct for the error in the 40 to 60 keV group. As stated above, the error is likely caused by the characteristic x-ray peaks in the incident x-ray spectrum. This is a relatively simple correction to make, and it should result in improved accuracy in this

important energy group.

5.3 Validation Stage

Although good verification data was obtained with TORT and MCNP, the validation was of less success. Much of the effort centered around capturing sufficient detail of the collimators and filters. Without these, the TORT and MCNP simulations estimated exposure and dose of the same order of magnitude as the measured results. However, with the collimator and bowtie included, the computed results were significantly better. The edge-to-center ratio computed was within the experimental error. The absolute exposures computed were within 35% of the measured values. These final validation exercises were performed with MCNP because of its superior flexibility. Through the validation process, the computational models have obtained a much greater level of realism, where they now begin to approach producing reasonable results. However, there is still much room to improve the models.

For further work Although some of the effects of the beam spectrum and the beam angular distribution were captured, there is no way of ensuring these are consistent with their actual experimental counterparts. Further improvement in the level of the computational models' validation demands more precise experimental measurements as well as some quantification of the discrepancy between the actual source spectrum and angular dependence compared to those employed by the computational models.

In addition, modeling the source in both MCNP and TORT became increasingly difficult, especially with the addition of the bowtie filter. The source could be inserted in MCNP by modifying the source code, but this exceeds the capabilities of the normal MCNP input. As for TORT, it is both more complex and simpler. Modeling the beam and collimation in TORT would be a challenge, more so than in MCNP. However, if the source could be transformed to an appropriate incoming boundary condition, TORT could handle this easily. Then the largest challenge would be computing the appropriate boundary flux, most likely bootstrapping a MCNP calculation at the boundary. A possible boundary of this sort is shown in Figure 4.3 as the dotted line. Since the phantom has negligible feedback on the source, the MCNP model should accurately capture the influence of the bowtie filter

on the incoming flux to the phantom. Defining an appropriate boundary source would also be a general method, suitable for the CTDI FDA phantom as well as the Rando phantom.

Bibliography

[1] J.K. Shultis and R.E. Faw. *Radiation shielding.* American Nuclear Society, 2000.

[2] W.C. Röntgen. On a New Kind of Rays. *Nature*, page 274, 1896. translated by Arthur Stanton.

[3] J.T. Bushberg, J.A. Seibert, E.M. Leidholdt Jr, J.M. Boone, and E.J. Goldschmidt Jr. The Essential Physics of Medical Imaging. *Medical Physics*, 30:1936, 2003.

[4] Willi A. Kalender. *Computed Tomography.* Wiley, 2000.

[5] L. A. Shepp. Scope of pure and applied tomography. In *Computed Tomography*, volume 27 of *AMS Short Course*, Cincinnati, Ohio, 1983. American Mathematical Society.

[6] J. G. Ravenel, E. M. Scalzetti, W. Huda, and W. Garrisi. Radiation exposure and image quality in chest CT examinations. *American Journal of Roentgenology*, 177:279–284, 2001.

[7] E. L. Nickoloff and P. O. Alderson. Radiation exposures to patients from CT: Reality, public perception, and policy. *American Journal of Roentgenology*, 177:285–287, 2001.

[8] Nationwide Evaluation of X-Ray Trends. 2001 survey of patient radiation exposure from computed tomography (CT) examinations in the United States. Technical report, U. S. Food and Drug Administration, Rockville, MD, 2001.

[9] J.L. Prince and J.M. Links. *Medical imaging signals and systems.* Pearson Prentice Hall, 2006.

[10] R. L. Morin, T. C. Gerber, and C. H. McCollough. Radiation dose in computed tomography of the heart. *Circulation*, 107:917–922, 2003.

[11] W. A. Kalender, B. Schmidt, M. Zankl, and M. Schmidt. A PC program for estimating organ dose and effective dose values in computed tomography. *European Radiology*, 9:555–562, 1999.

[12] R.D. Evans. *The Atomic Nucleus.* McGraw-Hill Education, 1955.

[13] J.E. Turner. *Atoms, Radiation, and Radiation Protection.* Wiley-VCH, 2007.

[14] Glenn F. Knoll. *Radiation Detection and Measurement.* John Wiley & Sons, 3rd edition, 2000.

[15] D. E. Ware, W. Huda, P. J. Mergo, and A. L. Litwiller. Radiation effective doses to patients undergoing abdominal CT examinations. *Radiology*, 210:645–650, 1999.

[16] P. C. Shrimpton and D. G. Jones. Normalised organ doses for x ray computed tomography calculated using monte carlo techniques and a mathematical anthropomorphic phantom. *Radiation Protection Dosimetry*, 49:241–243, 1993.

[17] J. P. Felmlee, J. E. Gray, Leetzow, M. L., and J. C. Price. Estimated fetal radiation dose from multislice CT studies. *American Journal of Roentgenology*, 154:185–190, 1990.

[18] E. K. Osei and K. Faulkner. Fetal doses from radiological examinations. *The British Journal of Radiology*, 72:773–780, 1999.

[19] M. F. Dietrich, D. L. Miller, and S.H. King. Determination of potential uterine (conceptus) doses from axial and helical ct scans. *Health Physics. Operational Radiation Safety.*, 88:S10–S13, February 2005.

[20] National Research Council. Committee on the Biological Effects of Ionizing Radiation. *Health Effects of Exposure to low levels of ionizing radiation, BEIR V.* National Academy Press, Washington, DC, 1990.

[21] E. E. Lewis and W. F. Miller, Jr. *Computational Methods of Neutron Transport.* American Nuclear Society, Inc., 1993.

[22] E.W. Larsen. The nature of transport calculations used in radiation oncology. *Transport Theory and Statistical Physics*, 26(7):739–763, 1997.

[23] WA Kalender, B. Schmidt, M. Zankl, and M. Schmidt. A PC program for estimating organ dose and effective dose values in computed tomography. *European Radiology*, 9(3):555–562, 1999.

[24] Los Alamos National Laboratory. *MCNP — A General Monte Carlo N-Particle Transport Code, Version 5*, April 2003.

[25] M. Caon, G. Bibbo, and J. Pattison. An EGS4-ready tomographic computational model of a 14-year-old female torso for calculating organ doses from CT examinations. *Physics in Medicine and Biology*, 44:2213–2226, 1999.

[26] G. Jarry, JJ DeMarco, U. Beifuss, CH Cagnon, and MF McNitt-Gray. A Monte Carlo-based method to estimate radiation dose from spiral CT: from phantom testing to patient-specific models. *Physics in Medicine and Biology*, 48(16):2645–2663, 2003.

[27] M.R. Ay and H. Zaidi. Development and validation of MCNP4C-based Monte Carlo simulator for fan-and cone-beam x-ray CT. *Physics in Medicine and Biology*, 50(20):4863, 2005.

[28] P. Deak, M. van Straten, P.C. Shrimpton, M. Zankl, and W.A. Kalender. Validation of a Monte Carlo tool for patient-specific dose simulations in multi-slice computed tomography. *European Radiology*, 18(4):759–772, 2008.

[29] H. Zaidi and M.R. Ay. Current status and new horizons in Monte Carlo simulation of X-ray CT scanners. *Medical and Biological Engineering and Computing*, 45(9):809–817, 2007.

[30] M. Caon, G. Bibbo, and J. Pattison. A comparison of radiation dose measured in CT dosimetry phantoms with calculations using EGS4 and voxel-based computational models. *Physics in Medicine and Biology*, 42:219–230, 1997.

[31] John M. Boone and J. Anthony Seibert. An accurate method for computer-generating tungsten anode x-ray spectra from 30 to 140 kv. *Medical Physics*, 24(11):1661–1670, 1997.

[32] AP Colijn, W. Zbijewski, A. Sasov, and FJ Beekman. Experimental validation of a rapid Monte Carlo based micro-CT simulator. *Physics in Medicine and Biology*, 49(18):4321–4333, 2004.

[33] R. A. Lillie, D. E. Peplow, M. L. Williams, B. L. Kirk, M. P. Langert, T. L. Nichols, and Y. Y. Azmy. Photon beam transport in a voxelized human phantom model: Discrete ordinates vs monte carlo. 14th Biennial Topical Meeting of the Radiation Protection and Shielding Division, pages 68–71, Carlsbad, NM, April 2006. American Nuclear Society.

[34] F. Inanc. A CT image based deterministic approach to dosimetry and radiography simulations. *Physics in Medicine and Biology*, 47(18):3351–3368, 2002.

[35] D. W. Nigg, P. D. Randolph, and F. J. Wheeler. Demonstration of three-dimensional deterministic radiation transport theory dose distribution analysis for boron neutron capture therapy. *Medical Physics*, 18:43–53, January 1991.

[36] D. W. Nigg, F. J. Wheeler, D. E. Wessol, J. Capala, and M. Chadha. Computational dosimetry and treatment planning for boron neutron capture therapy. *Journal of Neuro-Oncology*, 33:93–103, May 1997.

[37] D. T. Ingersoll, C. O. Slater, E. L. Redmond, II, and R. G. Zamenhof. Comparison of TORT and MCNP dose calculations for BNCT treatment planning. volume 75 of *Transactions of the American Nuclear Society*, pages 36–37, Washington, DC, Decemeber 1996. American Nuclear Society.

[38] Nuclear Associates: 76-414,76-414-4150,76-415, CT head and body dose phantom. Technical report, Fluke Biomedical, March 2005.

[39] Code of Federal Regulations, Title 21—Food and Drugs, Sec. 1020.33. Technical report, U.S. Food and Drug Administration, 2008.

[40] Alderson rando phantom systems for radiotherapy. Technical report, Alderson Research Laboratories, January 1969.

[41] X-ray spectrum of elements on the periodic table. Technical report, Lawrence Berkeley National Laboratory, Berkeley, CA, http://ie.lbl.gov/xray/, 2002.

[42] W. A. Rhoades and D. B. Simpson. *The TORT Three-Dimensional Discrete Ordinates Neutron/Photon Transport Code.* ORNL/TM-13221, 3rd edition, October 1997.

[43] R. Orsi. *BOT3P Version 5.0: A Pre/Post-Processor System for Transport Analysis.* ENEA Nuclear Data Center, April 2005. FIS-P9H6-008.

[44] R. E. MacFarlane and D. W. Muir. *The NJOY Nuclear Data Processing System, Version 91.* Los Alamos National Laboratory, October 1994. LA-12740-M.

[45] M.B. Chadwick, P. Obložinský, M. Herman, N.M. Greene, R.D. McKnight, D.L. Smith, P.G. Young, R.E. MacFarlane, G.M. Hale, S.C. Frankle, A.C. Kahler, T. Kawano, R.C. Little, D.G. Madland, P. Moller, R.D. Mosteller, P.R. Page, P. Talou, H. Trellue, M.C. White, W.B. Wilson, R. Arcilla, C.L. Dunford, S.F. Mughabghab, B. Pritychenko, D. Rochman, A.A. Sonzogni, C.R. Lubitz, T.H. Trumbull, J.P. Weinman, D.A. Brown, D.E. Cullen, D.P. Heinrichs, D.P. McNabb, H. Derrien, M.E. Dunn, N.M. Larson, L.C. Leal, A.D. Carlson, R.C. Block, J.B. Briggs, E.T. Cheng, H.C. Huria, M.L. Zerkle, K.S. Kozier, A. Courcelle, V. Pronyaev, and S.C. van der Marck. ENDF/B-VII.0: Next generation evaluated nuclear data library for nuclear science and technology. *Nuclear Data Sheets*, 107(12):2931–3118, December 2006.

[46] John C. Wagner, Everett L. Redmond II, Scott P. Palmtag, and John S. Henricks. *MCNP: Multigroup/Adjoint Capabilities.* Los Alamos National Laboratory, April 1994. LA-12704.

[47] T.R. Fewell, R.E. Shuping, K.R. Hawkins, United States Bureau of Radiological Health, and United States Bureau of Radiological Health. Division of Electronic Products. *Handbook of Computed Tomography X-ray Spectra.* US Dept. of Health and Human Services, Public Health Service, Food and Drug Administration, Bureau of Radiological Health, 1981.

[48] T. Toth, Z. Ge, and M.P. Daly. The influence of patient centering on CT dose and image noise. *Medical Physics*, 34:3093, 2007.

Appendices

APPENDIX A

Table *A*.1 is the mass coefficient data for the photon flux-to-exposure conversion.

Table A.1: Mass coefficients for dry air near sea level [1].

Energy (MeV)	μ_{en}/ρ (cm^2/g)
0.001	3599
0.0015	1188
0.002	526.2
0.003	161.4
0.0032	133
0.00321	146
0.004	76.36
0.005	39.31
0.006	22.7
0.008	9.446
0.01	4.742
0.015	1.334
0.02	0.5389
0.03	0.1537
0.04	0.06833
0.05	0.04098
0.06	0.03041
0.08	0.02407
0.1	0.02325
0.15	0.02496
0.2	0.02672
0.3	0.02872

APPENDIX B

Landauer provided reports of the results of the CT scan measurements taken at Hershey Medical Center. Figures B.1, B.2, and B.3 show the dose profile along the axis of the scan for the in air, CTDI center, and CTDI periphery.

LANDAUER® *Thinking Outside the Badge* ™

CT Dosimeter Report

CT Holder Number: 001605C1

Customer Information		Landauer Scanner Information	
Customer Facility:	HERSHEY MEDICAL CENTER	Process Number:	CT030308A
Account Number:	70152	Serial Number:	A0004127
Customer Contact:	STEVEN KING / BECKY ROBERTSON	Date Received:	3/3/08
Date Exposed:	1/3/08	Date Scanned:	3/5/08
kVp:	120	Dosimeter Scanner	1
mAs:	200	Slit Width (mm):	0.2
Phantom:	IN AIR	Sample Increment (mm):	0.05
Position in Phantom:		Smoothing Type:	20 PT AVE
Nominal Slice Width (mm):	1.5	Customer Comments:	
Number of Slices:	16	CT1, RUN #2	
Table Increment (mm):			
Total Table Travel (mm):			
Total Scan Length (mm):	139		
Scan Mode:	HELICAL		
Scanner Manufacturer:	SIEMENS		
Scanner Model:	SOMATOM SENSATION 16		

CT Dose Profile

(with 100 mm region of integration indicated with dashed lines)

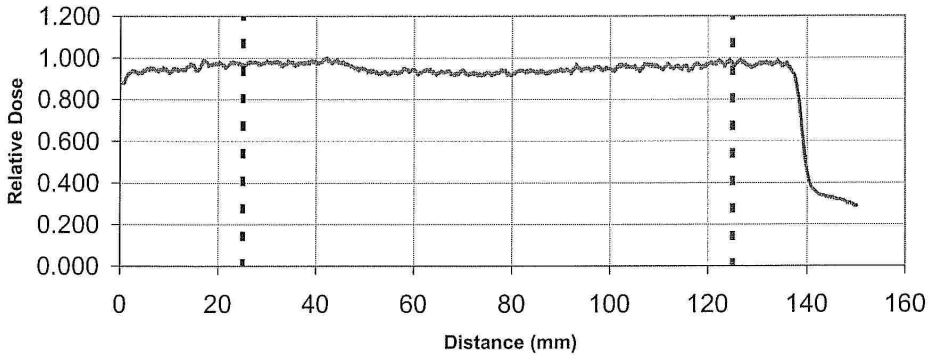

	Nominal	Observed
Total Integrated dose (mrad):	333724	
Slice Thickness (mm):	1.5	100
Number of Slices:	16	1

		mrad	*mGy*
$CTDI_{100}$ =	(333724) / (1.5 * 16) =	13,905	139.05

Figure B.1: The OSL dose measurement from Landauer for in air.

LANDAUER® *Thinking Outside the Badge* ™

CT Dosimeter Report

CT Holder Number: 001607CX

Customer Information

Customer Facility:	HERSHEY MEDICAL CENTER
Account Number:	70152
Customer Contact:	STEVEN KING / BECKY ROBERTSON
Date Exposed:	1/3/08
kVp:	120
mAs:	200
Phantom:	BODY / ABDOMEN
Position in Phantom:	CENTER
Nominal Slice Width (mm):	1.5
Number of Slices:	16
Table Increment (mm):	
Total Table Travel (mm):	
Total Scan Length (mm):	139
Scan Mode:	HELICAL
Scanner Manufacturer:	SIEMENS
Scanner Model:	SOMATOM SENSATION 16

Landauer Scanner Information

Process Number:	CT030308A
Serial Number:	A0004130
Date Received:	3/3/08
Date Scanned:	3/5/08
Dosimeter Scanner	1
Slit Width (mm):	0.2
Sample Increment (mm):	0.05
Smoothing Type:	20 PT AVE

Customer Comments:
CT1, RUN #8, CTR HOLE

CT Dose Profile

(with 100 mm region of integration indicated with dashed lines)

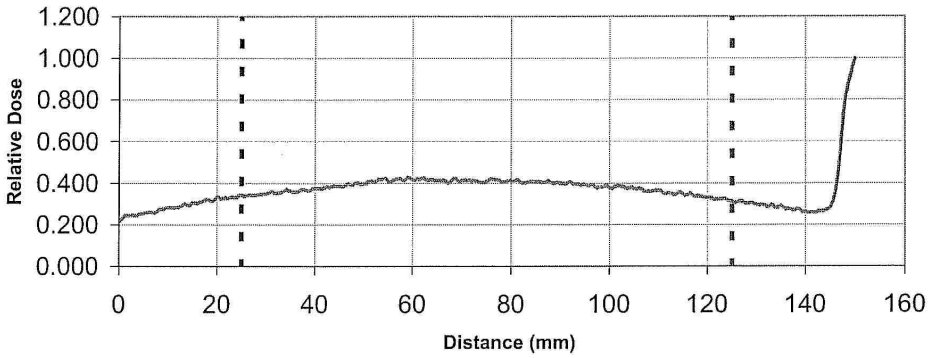

	Nominal	Observed
Total Integrated dose (mrad):	104643	
Slice Thickness (mm):	1.5	100
Number of Slices:	16	1

		mrad	*mGy*
$CTDI_{100}$ =	(104643) / (1.5 * 16) =	4,360	43.60

Figure B.2: The OSL dose measurements from Landauer for the CTDI FDA with the dosimeter in the center.

LANDAUER® *Thinking Outside the Badge™*

CT Dosimeter Report

CT Holder Number: 001606CZ

Customer Information

Customer Facility:	HERSHEY MEDICAL CENTER
Account Number:	70152
Customer Contact:	STEVEN KING / BECKY ROBERTSON
Date Exposed:	1/3/08
kVp:	120
mAs:	200
Phantom:	BODY / ABDOMEN
Position in Phantom:	TOP- 12:00
Nominal Slice Width (mm):	1.5
Number of Slices:	16
Table Increment (mm):	
Total Table Travel (mm):	
Total Scan Length (mm):	139
Scan Mode:	HELICAL
Scanner Manufacturer:	SIEMENS
Scanner Model:	SOMATOM SENSATION 16

Landauer Scanner Information

Process Number:	CT030308A
Serial Number:	A0004128
Date Received:	3/3/08
Date Scanned:	3/5/08
Dosimeter Scanner	1
Slit Width (mm):	0.2
Sample Increment (mm):	0.05
Smoothing Type:	20 PT AVE

Customer Comments:
CT1, RUN #7, TOP HOLE

CT Dose Profile

(with 100 mm region of integration indicated with dashed lines)

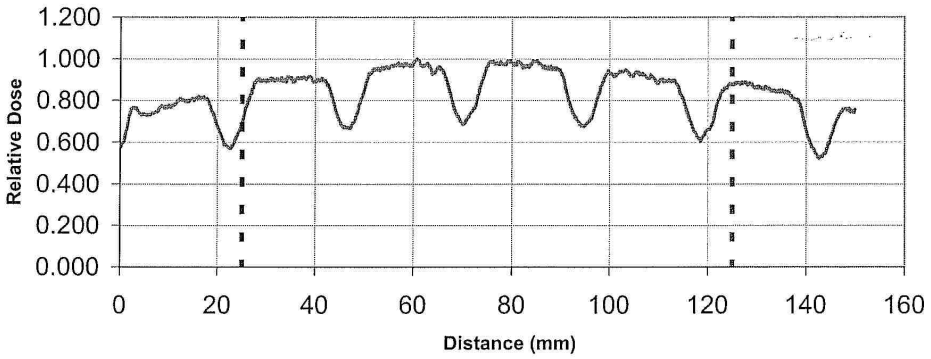

	Nominal	Observed
Total Integrated dose (mrad):	168611	
Slice Thickness (mm):	1.5	18.2
Number of Slices:	16	4

		mrad	*mGy*
$CTDI_{100}$ =	(168611) / (1.5 * 16) =	7,025	70.25

Figure B.3: The OSL dose measurement from Landauer for the CTDI FDA with the dosimeter in the periphery, 12 o'clock. Note the minima in dose, corresponding to the X-ray tube passing on the opposite side of the phantom.

APPENDIX C

The MCNP input file for the cylindrical, tissue equivalent phantom modeled for the determination of the importance of secondary electron transport follows:

```
Cylinder simplification to test p v. p e dependence
c  cognizant:      jmh
c  modified by kursat
c  date created:   09.17.06
c  date modified:  06.02.08
c
c  Cell cards
1  1 -0.997   -1 -3 4  #5 #6 IMP:P=1
2  0          1 -9 -3 4      IMP:P=1    $ air around cylinder,
c                                            inside source
3  0          9 -2 -3 4      IMP:P=1    $ source cell
4  0          2:3:-4         IMP:P=0    $ outside radiation source
5  1 -0.997   -5 -7 8        IMP:P=1    $ detector 1
6  1 -0.997   -6 -7 8        IMP:P=1    $ detector 2

c  Surface cards
1  CZ 13          $ cylinder
2  CZ 14          $ source cylinder
3  PZ 30          $ upper surface of cylinder
4  PZ -30         $ lower surface of cylinder
5  CZ 0.5         $ centerline detector
6  C/Z 6.5 0. 0.5 $ radial detector
7  PZ 1.27        $ upper surface of middle slice
8  PZ -1.27       $ lower surface of middle slice
9  CZ 13.99       $ source inner surface

c
c  Data cards
 MODE P
c
print
c
 PHYS:P 0.17
c
c  History limit
```

```
 NPS  1e10
c
c  Source definitions
c   collapsed cylinder to shell of radius 13.99-14.0
 SDEF  par=2 CEL=3 POS=0. 0. 0. axs=0. 0. 1. ext=D2  RAD=D1 erg=0.15
 SI1  13.99  14.0   $ inner and outer radii
 SI2  -30. 30.      $ lower and upper boundary of source shell
c
c  Material cards
c  define flesh material
 M1   1000.04P   -0.0918
      6000.04P   -0.6779
      7000.04P   -0.0250
      8000.04P   -0.2031
      51000.04P  -0.0022
c  Tallies
c  detector fluxes
F4:P 5           $ photon flux (calc by cell) in center
FC4 Photon flux (averaged over cell) in center.
F14:P 6           $ photon flux (calc by cell) in radius
FC14 Photon flux (averaged over cell) in radius.
E4  0.0  34I 0.17     $ Pulse height tally with 1 keV interval
E14 0.0  34I 0.17
c Energy deposition
F6:P     5        $ energy deposition
FC6 The energy dep. in the center.
F16:P    6        $ energy deposition
FC16 The energy dep. in the radius.
*F8:P     5        $ pulse height in center
*FC8 The energy dep. in the center.
*F18:P    6        $ pulse height in radius
*FC18 The energy dep. in the radius.
E6  0.0  34I 0.17     $ Pulse height tally with 1 keV interval
E16 0.0  34I 0.17
*E8  0.0  34I 0.17    $ Pulse height tally with 1 keV interval
*E18 0.0  34I 0.17
```

The following is an input for the nuclear data processing software NJOY which creates a ten group cross section set with weights according to the x-ray tube spectrum.

```
echo 'NJOY Processing of H for HMC Phantom'
cp ../../photoat/photoat-001_H_000.endf tape30
echo 'running njoy'
```

```
cat>input <<EOF
 moder
 30 -31
 reconr
 -31 -32
 'pendf tape for photon interaction cross sections from endfb-vii'/
 100 1 0
 .001 /
 '1-hydrogen'/
 0/
 gaminr
 30 -32 0 33
 100 1 1 3 1 /
 'multigroup xs for 1-hydrogen'/
 10 /
 0.0001 2+4 4+4 6+4 8+4 10+4 12+4 14+4 16+4 18+4 20+4 /
  0. 0. 0 0 1 95 95 2
  0 4.0-15
  10000 4.737223-15
  11000 1.233153-10
  12000 1.580334-07
  13000 2.523794-05
  14000 1.551920-03
  15000 3.890652-02
  16000 4.634538-01
  17000 4.033320+00
  18000 2.061618+01
  19000 6.125536+01
  20000 1.771197+02
  21000 3.754664+02
  22000 7.820547+02
  23000 1.346347+03
  24000 2.275612+03
  25000 3.478441+03
  26000 4.814198+03
  27000 6.496528+03
  28000 8.505339+03
  29000 1.042710+04
  30000 1.275927+04
  31000 1.479574+04
  32000 1.712696+04
  33000 1.903902+04
  34000 2.115740+04
```

```
35000 2.322475+04
36000 2.484371+04
37000 2.643248+04
38000 2.784517+04
39000 2.910465+04
40000 3.042166+04
41000 3.111268+04
42000 3.178604+04
43000 3.243634+04
44000 3.312011+04
45000 3.363410+04
46000 3.367801+04
47000 3.395713+04
48000 3.422125+04
49000 3.404143+04
50000 3.382571+04
51000 3.354899+04
52000 3.323626+04
53000 3.291855+04
54000 3.256915+04
55000 3.245482+04
56000 3.218550+04
57000 4.388305+04
58000 5.587529+04
59000 6.628486+04
60000 7.687260+04
61000 5.526577+04
62000 3.315936+04
63000 3.019739+04
64000 2.710519+04
65000 2.646874+04
66000 2.574225+04
67000 3.366806+04
68000 4.170096+04
69000 3.426603+04
70000 2.653623+04
71000 2.262850+04
73000 1.789171+04
74000 1.701548+04
75000 1.678377+04
77000 1.612864+04
79000 1.526176+04
80000 1.471177+04
```

```
 81000 1.433699+04
 83000 1.364756+04
 85000 1.270786+04
 87000 1.195702+04
 88000 1.170738+04
 90000 1.074090+04
 91000 1.034987+04
 92000 9.946510+03
 94000 9.050294+03
 95000 8.680247+03
 97000 8.015477+03
 100000 6.991587+03
 101000 6.682881+03
 103000 5.993847+03
 105000 5.245468+03
 108000 4.155511+03
 109000 3.826613+03
 110000 3.476991+03
 112000 2.759586+03
 114000 2.252646+03
 116000 1.503861+03
 118000 9.127958+02
 119000 6.155942+02
 120000 2.855908+02
 121000 9.714625+01
 200000. 9.7+1/
-1/
0/
dtfr
33 34 -31 36 /
1 1 0 /
4 10 3 4 13 1 0
'hydro'
1 525 1/
0 0 /
1 10 /
'h' 100 1 0/
/
stop
EOF
xnjoy <input
echo 'saving output and plot files'
cp output out_1_H
```

```
cp tape34 1H.dtf
```